The structure of the NuA4–Tip60 complex reveals the mechanism and importance of long-range chromatin modification

Alexander Fréchard, Céline Faux, Rozalie Hexnerova, Corinne Crucifix, Gabor Papai, Ekaterina Smirnova, Conor Mckeon, Florie Lo Ying Ping, Dominique Helmlinger, Patrick Schultz, et al.

Title: The structure of the NuA4/Tip60 complex reveals the mechanism and importance of long-range chromatin modification

Authors

Alexander Fréchard[1,2,3,4], Céline Faux[5], Rozalie Hexnerova[1,2,3,4], Corinne Crucifix[1,2,3,4], Gabor Papai[1,2,3,4], Ekaterina Smirnova[1,2,3,4], Conor McKeon[5], Florie Lo Ying Ping[5], Dominique Helmlinger[5], Patrick Schultz[1,2,3,4], Adam Ben-Shem[1,2,3,4]

Affiliations

[1] Institut de Génétique et de Biologie Moléculaire et Cellulaire, Integrated Structural Biology Department, Illkirch, France, Equipe labellisée Ligue Contre le Cancer.

[2]Centre National de la Recherche Scientifique, UMR7104, Illkirch, France.

[3]Institut National de la Santé et de la Recherche Médicale, U1258, Illkirch, France.

[4]Université de Strasbourg, Illkirch, France.

[5]Centre de Recherche en Biologie cellulaire de Montpellier (CRBM), Université de Montpellier, CNRS, Montpellier, France

Corresponding authors. Patrick Schultz (patrick.schultz@igbmc.fr), Adam Ben-Shem (adam@igbmc.fr) and Dominique Helmlinger (dhelmlinger@crbm.cnrs.fr)

Abstract

Histone acetylation regulates most DNA transactions and is dynamically controlled by highly conserved enzymes. The only essential histone acetyltransferase (HAT) in yeast, Esa1, is part of the 1MDa NuA4 complex, which plays pivotal roles in both transcription and DNA damage repair. NuA4 has the unique capacity to acetylate histone targets located several nucleosomes away from its recruitment site. Neither the molecular mechanism of this activity nor its physiological importance are known. Here we report the structure of the *Pichia pastoris* NuA4 complex with its core resolved at 3.4 Å resolution. Three subunits, Epl1, Eaf1, and Swc4, intertwine to form a stable platform that coordinates all other modules. The HAT module is firmly anchored into the core while retaining the ability to stretch out over a long distance. We provide structural, biochemical and genetic evidence that an unfolded linker region of the Epl1 subunit is critical for this long-range activity. Specifically, shortening the Epl1 linker causes severe growth defects and reduced H4 acetylation levels over broad chromatin regions in fission yeast. Our work lays the foundations for a mechanistic understanding of NuA4 regulatory role and elucidates how its essential long-range activity is attained. Our work lays

the foundations for a mechanistic understanding of NuA4 regulatory role and elucidates how its essential long-range activity is attained.

Introduction

The major histone H4 acetylase NuA4 comprises at least 12 subunits organized into four modules[1,2] and plays crucial roles in transcription regulation and DNA repair[3,4]. Esa1 forms a tetrameric histone acetyl transferase (HAT) module with the Eaf6, Epl1 and Yng2 subunits[1,2,5], whose structure was resolved by X-ray crystallography[6]. Esa1 promotes both targeted and untargeted H4 acetylation (Clarke, 1999; Reid, 2000). Targeted acetylation involves the NuA4 complex and occurs on specific promoters. Local recruitment of NuA4 can mediate long-range H4 acetylation patterns extending over several nucleosomes[7,8]. In *S. cerevisiae*, the HAT module exists also in isolation, separated from the other NuA4 subunits, to form the Piccolo complex. Piccolo, but not NuA4, promotes global, untargeted H4 acetylation[9,10]. The TINTIN module, composed of Eaf5, Eaf7, and Eaf3, a reader of methylated histone H3, forms a sub-complex regulating transcription elongation[11,12]. The 430 kDa Tra1 protein interacts with sequence-specific transcription activators and forms a module involved in NuA4 recruitment to gene promoters[1,13,14]. Tra1 is a member of the Phosphatidylinositol-3-Kinase-related Kinase (PIKK) family and is shared with the SAGA complex[15]. Although NuA4 and SAGA use the same activator-docking module, genome wide approaches revealed that they regulate both overlapping and distinct sets of genes, suggesting that activators can distinguish between SAGA and NuA4[16-18]. It is not known how the assembly and context of Tra1 within the two complexes affects activator binding. The NuA4 subunits Swc4, Yaf9 – a reader of acetylated histones, Arp4, and Act1 form a module also found in the SWR1 chromatin remodeling complex[19-21]. Arp4 and Act1 are also part of the INO80 ATP-dependent chromatin. The four modules are thought to be connected by a single scaffolding component, Eaf1, the only NuA4 subunit that is not shared with another chromatin modification/remodeling complex or with Piccolo[10,11,22].

Structure of isolated subunits or modules have been reported[6] but structural information regarding holo-NuA4 is limited to intermediate resolution EM reconstructions[11,23]. These revealed an L-shape assembly where the Actin and Tra1 modules each occupy a different domain while the HAT and TINTIN modules are poorly resolved. Moreover, the scaffold that orchestrates the binding and activity of the other modules within NuA4 could not be revealed. Importantly, and in contrast to the major H3 acetyltransferase SAGA, NuA4 is able to act over thousand base-pairs (kbp) away from its recruitment site[7,8]. First, the Workman group showed a difference in acetylation range between NuA4 and SAGA *in vitro*[8]. Using purified complexes targeted to a discrete site on a chromatin template through GAL4 binding sites and a Gal4-VP16 activator, they found that NuA4 generates a broader acetylation prolife than SAGA, extending over 1.5 kb from the site of recruitment, whereas SAGA can only acetylate adjacent nucleosomes. Second, the Struhl group measured H4 acetylation levels at ribosomal protein (RP) genes *in vivo* using chromatin immunoprecipitation followed by quantitative PCR (ChIP-qPCR), and found that the NuA4-dependent H4 acetylation is detected over 800 bp upstream

and downstream of NuA4 binding within the promoter[7]. Hence fundamental questions remain unanswered, including how the HAT activity is embedded within the complex and how it targets nucleosomes located at a distance. More generally, other chromatin modifying complexes are suspected to possess long-range activity, however the mechanism and functional relevance of such an activity remain elusive[24,25].

Here we report the structure of NuA4 at 3.4 Å resolution. Clear amino acid densities allowed us to fully trace the core of the complex. We reveal how a scaffold composed of extended and interwoven Eaf1, Epl1 and Swc4 subunits tightly binds Tra1, as well as the actin module, coordinates several flexible histone-tail readers, and incorporates the HAT module. Most importantly, a long, unfolded region of Epl1 connects an alpha helix embedded in the core of NuA4 with the N-terminus of Epl1, which is an integral part of the HAT module. We show that this region endows the HAT module with its long-range action relative to NuA4 core and that this capacity is critical for fission yeast proliferation and bulk histone H4 acetylation *in vivo*. Finally, using ChIP-qPCR, we observed a reduction in H4 acetylation levels over extended genomic regions, spanning several kilobases, when the Epl1 linker was shortened, demonstrating its importance in establishing broad domains of H4 acetylation *in vivo*.

Overall structure

NuA4 complex was purified from a strain of the budding yeast *Pichia pastoris* (*Pp*) carrying a Streptavidin Binding Protein (SBP) affinity-tag fused to the endogenous Eaf1 subunit. The complex contained 12 subunits with a composition that differs from *S. cerevisiae* only in the TINTIN module[12], which harbors a "reader" domain of histone-tail modifications (Extended Data Fig.1). In *P. Pastoris*, TINTIN lacks subunits Eaf5 and Eaf3 that recognizes a methylated histone, but contains instead a homologue of the human BRD8 component of TINTIN, that binds acetylated histones[26,27] (Extended Data Fig.2). These variations may reflect the plasticity of the NuA4 reader domains to adjust to specific epigenetic regulation mechanisms.

The structure of holo-NuA4 at 3.4 Å resolution was determined by single particle cryo-electron microscopy (cryo-EM) while focused refinement and classification improved the resolution for the core of the complex to 3.3 Å (Fig. 1a, Extended Data Figs. 3 and 4, Extended Data Table 1). The high quality of the map showed clear density for the majority of side chains in the core and enabled constructing a nearly complete atomic model for this part (Fig 1b, Extended Data Fig. 5). The core is composed of the Tra1 module on which the actin Arp4-Act1 hetero-dimer, bound to the Swc4 SANT-like domain, is grafted by means of a scaffolding neck formed by intertwining Eaf1, Swc4, and the C-terminal half of Epl1 which connects to the HAT module (Fig. 1c). The clear delineation of the C-terminal half of Epl1 subunit in the core, guided by densities for amino acid side chains, indicates that Epl1 is present in the vast majority of NuA4 particles. However, the N-terminal part of Epl1, and the HAT module organized around it[9], are not readily detected in our cryo-EM map, indicating that the HAT module is inherently mobile relative to the core, as described below. Such movements probably also explain why the nucleosome binding Yaf9 subunit as well as the TINTIN module are not discernible in the map. In sharp contrast, the Epl1 and Swr4 SANT domains, which can also bind nucleosome core

particles or unmodified histone tails, are very stable. Hence, NuA4 employs both flexible and static modes of interaction with a nucleosomal substrate.

Epl1, Swr4 and Eaf1 subunits form a stable scaffold

An intricate path of the Eaf1 subunit could be traced unambiguously in our map as it traverses the neck of NuA4 multiple times (blue colored subunit, Fig. 1b and d). With the exception of the SANT domain, Eaf1 is mostly organized into loops, stretches of unfolded domains and isolated helices. Epl1 and Swc4 are both elongated and extended proteins that interact with Eaf1 extensively along the neck, from Tra1 to the actin module, and support the highly intricate topology of Eaf1 (Fig. 1b). Following a disordered N-terminal stretch that anchors the TINTIN module[23], Eaf1 makes critical contacts with Tra1, then continues towards the neck base where it forms a beta-sheet stabilized by three strands contributed by Epl1 ($Eaf1^{1}$ in Fig. 1b and d). Eaf1 continues by providing two long helices to the bundle forming the bulk of the neck base and the loop between the two helices binds again to Tra1 ($Eaf1^{2}$). Eaf1 then folds into the helicase-SANT-associated ($Eaf1^{HSA}$) helix, which firmly binds the Actin module and is followed by a 12-residue long loop that partially encircles Act1 ($Eaf1^{3}$, Fig. 1e). The engagement of the Actin module is further bolstered by the Swc4 SANT-like domain as well as two strands and a helix from Epl1 that associate with the HSA helix and Arp4, respectively. Eaf1 traverses the neck domain a fourth time completing the Eaf1/Epl1 beta sheet with an additional beta-strand ($Eaf1^{1}$). The C-terminal part of Eaf1 connects to three distinct sites on Tra1 via its SANT domain ($Eaf1^{SANT}$), as well as two additional helices, virtually encircling the FAT domain of Tra1 ($Eaf1^{4}$ in Fig. 1b and d). These two helices form an important hub of inter-module contacts. In addition to Tra1, they bind a helix of Swc4 that immediately precedes the domain anchoring Yaf9 and, most importantly, they also connect to the first helix of Epl1 in the core (helix H1). This Epl1 helix is preceded by a long, unfolded linker and the N-terminal half of Epl1 that is part of the HAT module. Hence, a major site of neck binding to the Tra1 module also associates with the domains of Swc4 and Epl1 that coordinate Yaf9 and the HAT module, respectively. The most prominent structured part of the neck is a helix bundle that forms strong contacts with Tra1 and where all three scaffolding subunits intertwine. Epl1 contributes two helices that envelope two Eaf1 helices ($Eaf1^{2}$), and Swc4 completes the bundle with a long, kinked helix. Multiple strong interactions, including hydrophilic and hydrophobic bonds stabilize this helix bundle which provides stability and stiffness to the scaffolding neck. Altogether, Eaf1 contacts six proteins from all modules of NuA4 in accordance with its proposed scaffolding role[22]. However, Eaf1 is highly extended, and contains a large proportion of unfolded loops that would not be sufficient to construct a stable interaction platform. Our results highlight the essential contributions of Epl1 and Swc4 to shaping the architecture of NuA4, since only an extensive interaction network between these components and Eaf1 provides a robust platform to stably anchor the functional modules.

The unique environment of the actin module

An actin hetero-dimer is found in several chromatin re-modelers, in which it binds a long HSA helix and forms a mobile module poorly resolved in EM maps. Conversely, in the head part of NuA4, the Eaf1^{HSA}-Act1-Arp4 module is strongly coupled to the neck and is well resolved. This stability stems from multiple additional interactions between this module and the SANT-like domain of Swc4, an Epl1 loop that intercalates between the two actin proteins, as well as a loop from Eaf1 (Extended Data Fig. 6). This complementary interaction network completely envelopes and shields the Eaf1^{HSA} helix, which is unlikely to play a role similar to its analogue in the INO80 complex, where it serves as a long-range sensor for extra-nucleosomal DNA[28]. The nearly neutral charge of the Eaf1^{HSA} helix also supports this conclusion. Hence the role of the actin module in NuA4 remains enigmatic but, at least in part, it seems that the actin module and Tra1 serve an important structural role by stabilizing and constraining the three scaffolding subunits at each extremity of the neck.

Ensuring selective use of Tra1

The large ~400 KDa Tra1 subunit is the only component shared between NuA4 and the SAGA H3 acetyltranferase, thus raising questions about the mechanism governing incorporation of specific subunits into either complex, while preventing formation of chimeric assemblies between SAGA and NuA4[27]. The central module of SAGA associates with Tra1 through three main protein bridges[24,29]. We find that Eaf1 interactions with Tra1 engage all sites occupied by these bridges (Fig. 2a). In one case, the bridge formed by Eaf1 and Tra1 structurally mimics the analogous binding surface in SAGA, as an Eaf1 loop sends an aromatic residue (F523) protruding into the Tra1 ring as observed for Spt3 within SAGA. Thus, binding of Eaf1 is sufficient for nucleating Tra1 into NuA4 (Fig. 2a).

Tra1 serves as the major docking platform for activators that recruit SAGA and NuA4 to specific promoters[13]. However, many genes are predominantly regulated by either NuA4 or SAGA in yeast[17,27] and the affinity between each complex and certain activators differ *in vitro* [13]. Our structure offers some clues to understand these functional differences. NuA4 forms more extensive interactions with Tra1 involving not only Eaf1, that practically envelops the Tra1 FAT domain, but also Swc4 and Epl1 contributions, mainly from the helix bundle at the neck base (Fig. 2b). Moreover, the NuA4 neck is tilted by 90° as compared to SAGA, resulting in distinct Tra1 surfaces accessible to activators. Additionally, bridge forming subunits might play auxiliary roles in activator binding[30] and further differentiate the two complexes. Lastly, we observe differences between the two complexes in the flexibility of some internal domains of Tra1 (Fig. 2c, Extended Data Fig. 7). The LBE/FRB module of the Tra1 pseudo kinase is better ordered in NuA4 where it may be stabilized by the N-terminal Eaf1 helix (residues 167-173) interacting next to the FRB domain. Conversely, 9 helices forming the Tra1

ring solenoid (residues 2110-2322) show significant better local resolution in SAGA than in NuA4 indicating a higher mobility of the corresponding NuA4 HEAT repeats. Collectively, these effects may contribute to form specific activator binding interfaces within each complex.

Uncovering the HAT module

We next sought to resolve how the HAT module is connected to the core. It was previously shown that the N-terminal half of Epl1 is part of the HAT module whereas the C-terminal half, which we resolved in the core, is crucial for its inclusion into NuA4[9]. Focussed classification within a sphere expanding from the first Epl1 residue detected in our map revealed a fuzzy density that was only apparent at low density threshold, suggesting that the HAT module is flexibly attached to NuA4. We posited that mobility is likely to be conferred by a stretch of amino acids predicted to be disordered (residues 359-418). This linker is conserved between yeasts and vertebrates (Extended Data Fig. 8) and connects the last Epl1 residue resolved in the crystal structure of the HAT module (K358) with the first residue discernible in our cryo-EM map (M419). This residue is closely followed by the first Epl1 helix in the core (Helix H1, S431). We introduced a TEV protease cleavage site into the linker to investigate its role in connecting the HAT module to the core. Using an SBP affinity-tag on Eaf1, holo-NuA4 was bound to streptavidin beads and then incubated with TEV protease. We observed that all HAT subunits were efficiently and specifically released from holo-NuA4 upon cleavage, demonstrating that the HAT module is tethered to the core mainly by the long unstructured Epl1 linker (Extended Data Fig. 9). This observation agrees with cross-linking coupled to mass spectrometry analyses, which identified only a few interactions between the HAT module and the core[23].

To better visualize the HAT module connected to NuA4, deletion mutants were designed to gradually shorten the linker (Epl1-SL1, Epl1-SL3, Epl1-SL5) and bring the HAT module closer to the core (Fig. 3a). The fuzzy density indeed grew bigger and drew nearer to the core as the loop got shorter. The density corresponding to deleted residues was no longer observed in the core, further supporting our Epl1 density assignment and residue register (Fig. 3b). Furthermore, neural network-based heterogeneity analysis (cryoDRGN) of the WT and the Epl1-SL1 and Epl1-SL3 mutants showed clearly that a density with the size of the HAT module appears close to the core in 90% of the Epl1-SL3 images, whereas such adjacent density was observed in only 10% of the WT images (Fig. 3c). This analysis shows that shortening the Epl1 linked attracts a protein density close to NuA4 core. Although residual flexibility precluded the resolution of molecular details, the appended domain is connected to the Epl1 H1 helix in representative classes (Fig. 3d). To gain insights into its molecular shape, particles were re-centred on the attached density and the signal of core NuA4 was subtracted. *Ab initio* 3D reconstruction and heterogeneous refinement of the residual domain resulted in a cryo-EM map at 11.5 Å resolution highly similar in shape to the crystal structure of the HAT module[6] (Fig. 3e). An extra protein density is detected in the cryo-EM map and may correspond to parts not included in the crystal structure. Altogether these experiments demonstrate that the HAT

module is tethered to the Epl1 H1 helix within the core of NuA4 via a long unstructured Epl1 linker that determines its orientation and maximal distance from the core (Fig. 3f)

To test whether Esa1 enzymatic activity is regulated by the Epl1 linker, mutant NuA4 complexes containing short linkers were affinity-purified and their ability to acetylate nucleosome core particles was assayed by Western blot analysis (Fig. 3g). These results show that the Epl1 short linker mutants are enzymatically as active as WT NuA4 and are able to modify a diffusing mono-nucleosomal substrate *in vitro*. Hence, reducing the Epl1 linker length does not affect the intrinsic enzymatic activity of Esa1.

A long linker is essential for viability in *S. pombe*

We next examined the function of the unstructured Epl1 linker *in vivo*. For this, we switched to *S. cerevisiae* because of its amenability for genetic manipulation. As *EPL1* deletion is lethal[31], we created *epl1* linker mutants in a *sds3*Δ deletion background, which suppresses NuA4 null mutants[32]. Tetrad analysis of heterozygous diploid mutants demonstrated that the Epl1-SL3 and Epl1-SL5 mutants cause neither over growth phenotypes nor defects in bulk histone H4 acetylation levels (Extended Data Fig. 10). Epl1-SL5 mutants, which have the longest linker deletion, display mild sensitivity to high temperature, suggesting defects in targeted, activator-driven H4 acetylation and transcriptional induction. However, biochemical and genetic evidence indicate that incorporation of the HAT module into NuA4 is not essential in *S. cerevisiae* because of the existence of a free version of the HAT module, named Piccolo[9,10,32]. Indeed, deletion of either the scaffolding subunit Eaf1 or of the Epl1 C-terminal half is viable. Our result supports this model and suggest that Piccolo masks the putative effects of Epl1 linker shortening.

In marked contrast, in the distantly related fission *Schizosaccharomyces pombe*, the Eaf1 homologue Vid21 is essential for viability, despite similar subunit composition[27,33](Extended Data Fig. 1). We thus reasoned that, rather than Piccolo, the holo-NuA4 complex is critical for proliferation in fission yeast. Accordingly, we observed that deleting the C-terminal end of *S. pombe* Epl1 causes lethality (Extended Data Fig. 11), whereas an analogous truncation mutation detaches the HAT module from holo-NuA4 and is viable in *S. cerevisiae*[9]. Thus, unlike *S. cerevisiae*, incorporation of the HAT module into NuA4 is essential in *S. pombe*.

This finding prompted us to test the importance of the distance between the HAT module and the core-NuA4 in this yeast. To introduce conditional mutations at the endogenous *epl1*+ locus, we implemented a novel strategy based on a Cre recombinase-dependent "flip-excision" switch (FLEx), initially developed in mice[34](Fig. 4a). Briefly, FLEx takes advantage of the β-estradiol inducibility of a Cre-ER fusion, the ability of Cre to either invert or excise a DNA fragment depending on the orientation of the flanking lox sites, and the existence of lox variants that are not cross compatible. We obtained three Epl1-FLEx mutants, Epl1-SL1, -SL5, and -DCt (Fig. 4b). PCR of genomic DNA and marker analyses revealed that β-estradiol addition induces a rapid, efficient, and irreversible inversion of the *epl1* locus, demonstrating the utility of this approach for conditional genetic manipulation in *S. pombe* (Fig. 4c-d).

Remarkably, we observed β-estradiol-induced proliferation defects leading to strong reduction in *S. pombe* viability in both the *epl1-SL1* and *-SL5* FLEx mutants (Fig. 4d-e). As expected from our tetrad analyses, we observed a similar phenotype in the *epl1-DCt-FLEx* strain, validating the FLEx approach. These results demonstrate that the length of the Epl1 linker has critical functions in *S. pombe* proliferation. Finally, Western blot analyses of total protein extracts showed that the Epl1-DCt, Epl1-SL1, and Epl1-SL5 mutants are stably expressed and confirmed that β-estradiol induces a robust switch from wild-type MYC-tagged Epl1 to the three HA-tagged mutant forms (Fig. 4f).

The Epl1 linker is required for long-range H4 acetylation

We then tested the effect of shortening the *S. pombe* Epl1 linker on histone H4 acetylation. Western blot analysis of total protein extracts revealed a modest, but reproducible reduction of normalized H4 acetylation levels in both the *epl1-SL1-FLEx* and *epl1-SL5-FLEx* mutants, as compared to uninduced conditions and to WT control strains, suggesting that shortening the Epl1 linker affects NuA4 activity *in vivo* (Fig. 5a). Semi-quantitative analyses of signal intensities indicated that the longer truncation mutant, Epl1-SL5, has a stronger effect than the shorter mutant, Epl1-SL1, as compared to a complete loss of Epl1 C-terminal moiety (Fig. 5b). Together with our finding that the Epl1 linker does not regulate the intrinsic enzymatic activity of Esa1 *in vitro*, these results indicate that the distance between the HAT module and the core NuA4 is important for bulk H4 acetylation *in vivo*. We next used chromatin immunoprecipitation followed by quantitative PCR (ChIP-qPCR) to measure H4 acetylation at chromatin in conditional *epl1-SL5* mutants. Specifically, we examined three distinct loci, including the *adh1* gene, which has a 2kb-long upstream intergenic region, the highly expressed *mmf1* and *rpl1603* genes, and part of the subtelomeric region of chromosome II right arm, which only contains pseudogenes and the repressed *tlh2* gene (Fig. 5c-e). Overall, at all loci, we observed a reproducible decrease of H4 acetylation levels normalized to total H3, as compared to uninduced conditions. Notably, at the *adh1* locus, this reduction is apparent both in the coding region and over 1kb upstream of the transcription start site (TSS, +1), but not within 500 bps upstream of the TSS (Fig. 5c), which is where NuA4 presumably binds to chromatin through activator recruitment. Likewise, H4 acetylation levels decrease where NuA4 likely does not bind. First, we observed reduced H4 acetylation levels over the coding region of the *mmf1* and *rpl1603* genes, including towards their 3' ends (Fig. 5d). Second, we show that shortening the Epl1 linker reduces basal H4 acetylation levels over an extended region of a subtelomeric region, spanning several kilobases, and containing only the repressed genes and pseudogenes (Fig. 5e). Overall, these observations are consistent with a model by which, in *S. pombe*, the Epl1 linker endows NuA4 with the ability to acetylate histone H4 over large nucleosomal domains.

Conclusion

In vitro experiments show that NuA4 has the capacity to find its targets over long distances, contrary to SAGA, in which the HAT module is directly coupled to the core via a structured domain[8]. Specifically, distinct histone acetylation patterns were observed upon using an activator to recruit either SAGA or NuA4 to an artificial promoter. While SAGA acetylates H3

from nucleosomes immediately adjacent to the activator binding site, NuA4 generates a broader H4 acetylation profile, extending up to 1.5 kbp, which corresponds to 7-8 nucleosomes.

In vivo observations further support the long-range activity of NuA4. First, ChIP-qPCR analyses show that, in *S. cerevisiae*, Esa1-dependent H4 acetylation spans an entire gene encoding a ribosomal protein, including the promoter and coding sequences, although NuA4 is specifically recruited to the activator binding-sites within the promoter[7]. Second, NuA4 is recruited to the upstream region of the *PHO5* gene promoter, through interactions with Pho2, but contributes to chromatin remodeling spanning 4 nucleosomes[35]. We show here that the distance between the HAT module and the rest of the complex is important for yeast proliferation and contributes to maintain basal H4 acetylation levels in *S. pombe*. Furthermore, our ChIP assays show that shortening the Epl1 linker does not affect H4 acetylation levels proximal to the NuA4 recruitment sites within the promoter, but decreases distal H4 acetylation in the gene body. Altogether, our work describes the mechanism that endows a chromatin-modifying enzyme with long-range activity and provides evidence for the importance of this function *in vivo*. We note that the length of the Epl1 linker varies between species (Extended Data Fig. 8c), ranging from 50 residues in *S. pombe* up to 109 residues in *S. cerevisiae*. It is thus likely that the theoretical physical reach changes between species. One possible explanation for these variations might relate to differences in nucleosome spacing. Notably, the linker length is shorter in *S. pombe* than in *S. cerevisiae*, suggesting that, in the latter, NuA4 can reach longer distances to modify a given number of nucleosomes[36,37]. Finally, other chromatin modifying enzymes, including the histone deacetylase Sin3L/Rpd3L co-repressor complex[25], have unstructured protein domains linking the enzymatic modules to the core of the complex. We suggest that for these enzymatic complexes, a similar mechanism allows histone modifications to be deposited at long distances from the recruitment site.

Acknowledgements:

We are grateful to Simonetta Piatti and Lorraine Pillus for kindly sharing *S. cerevisiae* strains. We thank the mass spectrometry service of the IGBMC for helpful advises and the Nanotumor Consortium, with financial support from ITMO Cancer of AVIESAN (National Alliance for Life Sciences & Health) within the framework of the Cancer Plan, for helpful discussions. We acknowledge support from the Institut National de la Santé et de la Recherche Médicale (INSERM), the Centre National pour la Recherche Scientifique (CNRS), the ITMO Cancer of AVIESAN (National Alliance for Life Sciences & Health) within the framework of the Cancer Plan, the Ligue contre le Cancer, the University of Strasbourg Institute for Advanced Study (USIAS) for a fellowship to P.S. within the French national program “investment for the future” (IdEx-Unistra), the Agence Nationale de la Recherche (ANR) grants ANR-17-CE12-0022 to P.S., ANR-15-CE11–0022–03 to D.H., and ANR-10-LABX-0030-INRT to IGBMC. We acknowledge the use of resources of the French Infrastructure for Integrated Structural Biology FRISBI ANR-10-INBS-05 and of Instruct-ERIC. With financial support from

Author contributions:

A.B.S., DH and P.S. designed the study; A.B.S originated the NuA4 purification method; A.B.S. and C.C. defined conditions for grid preparation and freezing; C.C., A.F. and G.P. prepared cryo-EM specimens; G.P. collected and A.F. analyzed cryo-EM data; A.F. and A.B.S. interpreted the maps by fitting crystal coordinates and model building; E.S. and R.H. performed HAT activity assays, F.L.Y.P., C.M.K. and C.F. performed all *S. cerevisiae* and *S. pombe* experiments, D.H., P.S. and A.B.S. supervised the work; D.H., A.F. and P.S. prepared figures; A.B.S., D.H., A.F., and P.S. wrote the manuscript with inputs from all authors.

Competing Interests Statement:

The authors declare no competing financial interest.

Figures legends

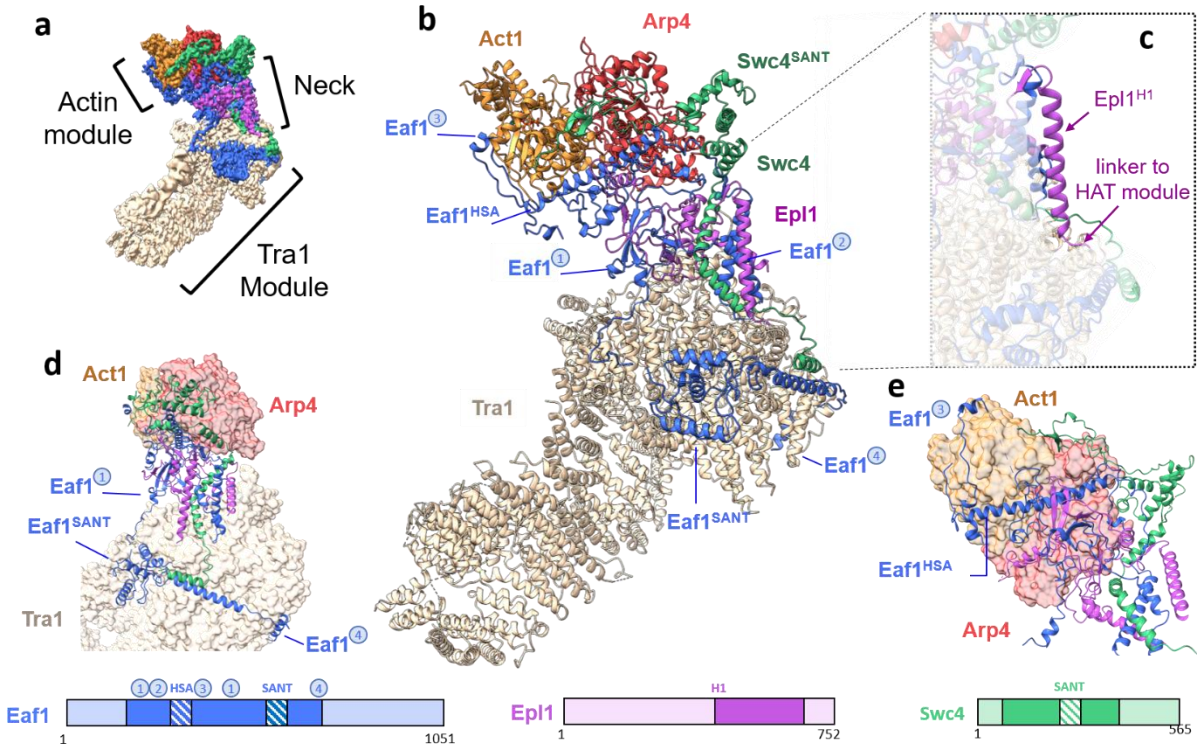

Figure 1 | Structure of the yeast NuA4 core complex. **a**, Side view of the composite cryo-EM reconstruction of the *P. pastoris* NuA4 core complex. Maps from focused refinements of the Tra1, Neck and Actin modules were combined. **b**, Corresponding view of the atomic model of the NuA4 core complex. **c**, Detailed view of the Epl1 H1 helix and the end of the linker that connects to the HAT module. **d**, Structural organization of the neck region that connects the actin module to the Tra1 module. **e**, Detailed bottom view of the connection to the actin module.

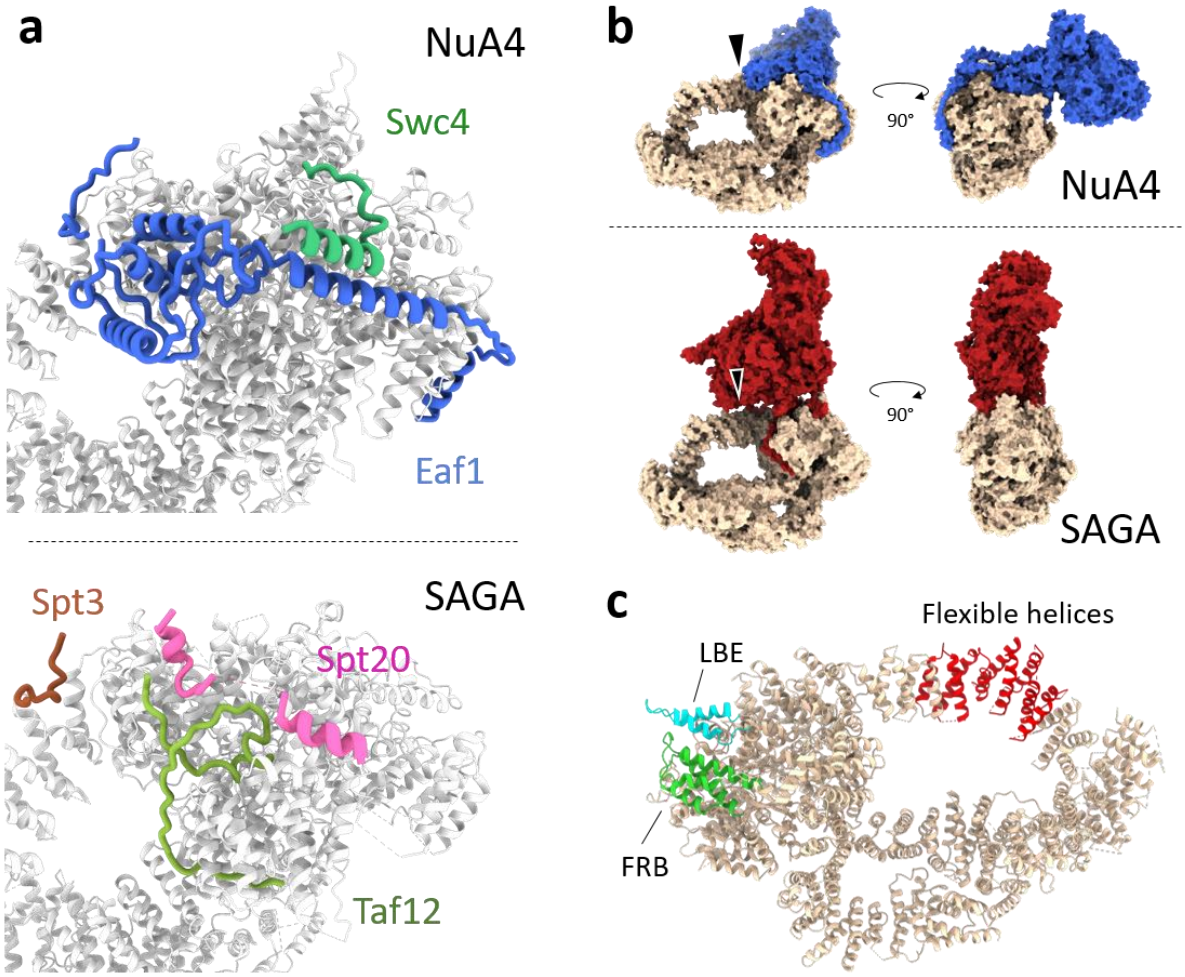

Figure 2 | Ensuring selective use of Tra1. **a**, Close-up view of the structural elements that contact Tra1 in NuA4 (upper panel) and in SAGA (lower panel). The two views are identical, differences in Tra1 structure are due to changes in its conformation or flexibility when incorporated in NuA4 as compared to SAGA**. b**, Position of Tra1 with respect to the rest of the NuA4 (upper panel) or SAGA (lower panel) subunits. The Tra1 subunits have been aligned one with respect to the other. **c**, The Tra1 pseudokinase regulatory domains LBE (blue) and FRB (green) are less flexible in NuA4 than in SAGA, while the HEAT repeats highlighted in red are more disorganized in NuA4 than in SAGA.

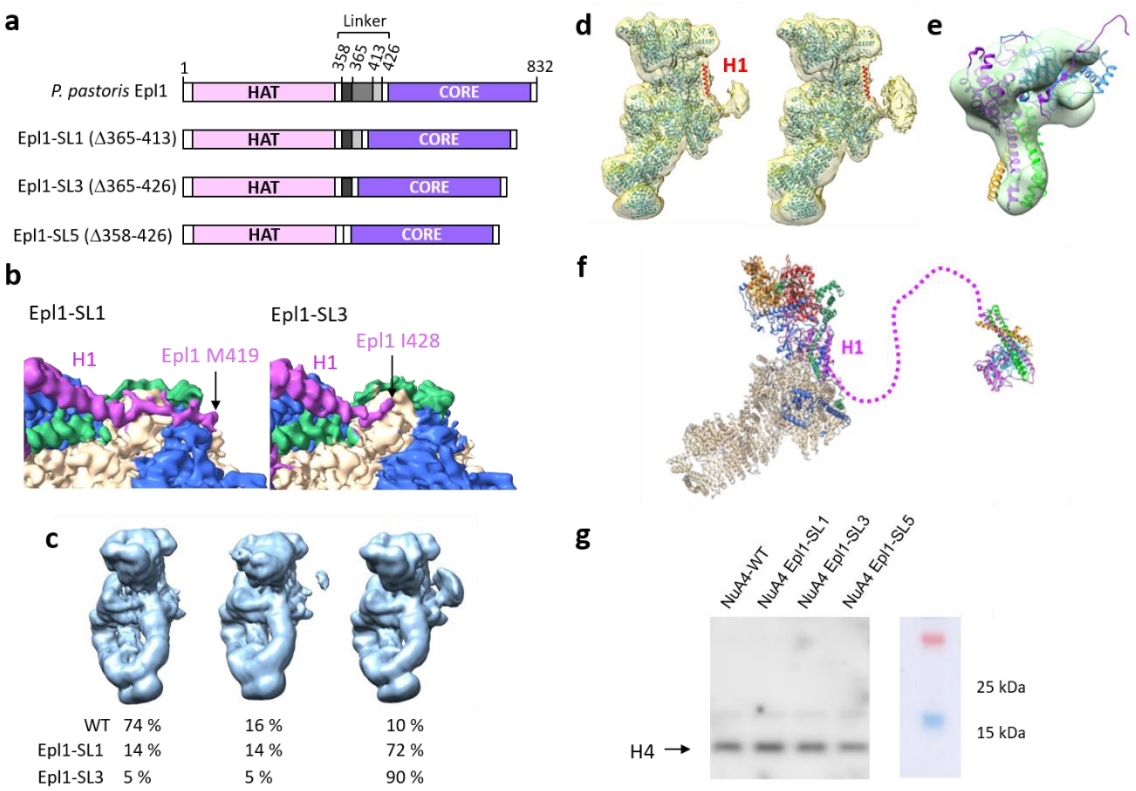

Figure 3 | Shortening the Epl1 linker uncovers the HAT module. a, Linker deletion mutants used in this study. The Epl1 subunit is organized into an N-terminal half inserted into Piccolo (pink), and a C-terminal half revealed in NuA4 core (violet). The two Epl1 halves are connected by a disordered linker (grey). **b**, Cryo-EM maps of the Epl1-SL1 (left panel) and the Epl1-SL3 (right panel) mutants highlighting the Epl1 H1 helix and the start of the linker that is shortened in the Epl1-SL3 mutant. **c,** Representative cryoDRGN classes lacking the HAT module (left), with hints of the HAT module (middle) or with clear attached HAT module (right). These three categories are found in all three datasets (WT, Epl1-SL1 or Epl1-SL3), but with different frequencies. The numbers below the cryo-EM maps show for each Epl1 linker length the proportion of particles found in each category**. d**, Two representative cryoDRGN classes of the Epl1-SL3 mutants showing the attached HAT module. **e**, Three-dimensional reconstruction of the density attached next to helix H1 in the Epl1-SL5 mutant. The signal of core-NuA4 was subtracted from each Epl1-SL5 particle and the residual density was reconstructed *ab initio*. The atomic structure of Piccolo (PDB 5J9U) has been docked into this density (green). **f**, Model of Piccolo linked to core NuA4. The dashed line represents the Epl1 linker in its fully extended form corresponding to 33 nm. **g**, HAT activity of NuA4 with different linker lengths on nucleosome core particles. Molecular weight marker (M). Arrow highlights the H4 band.

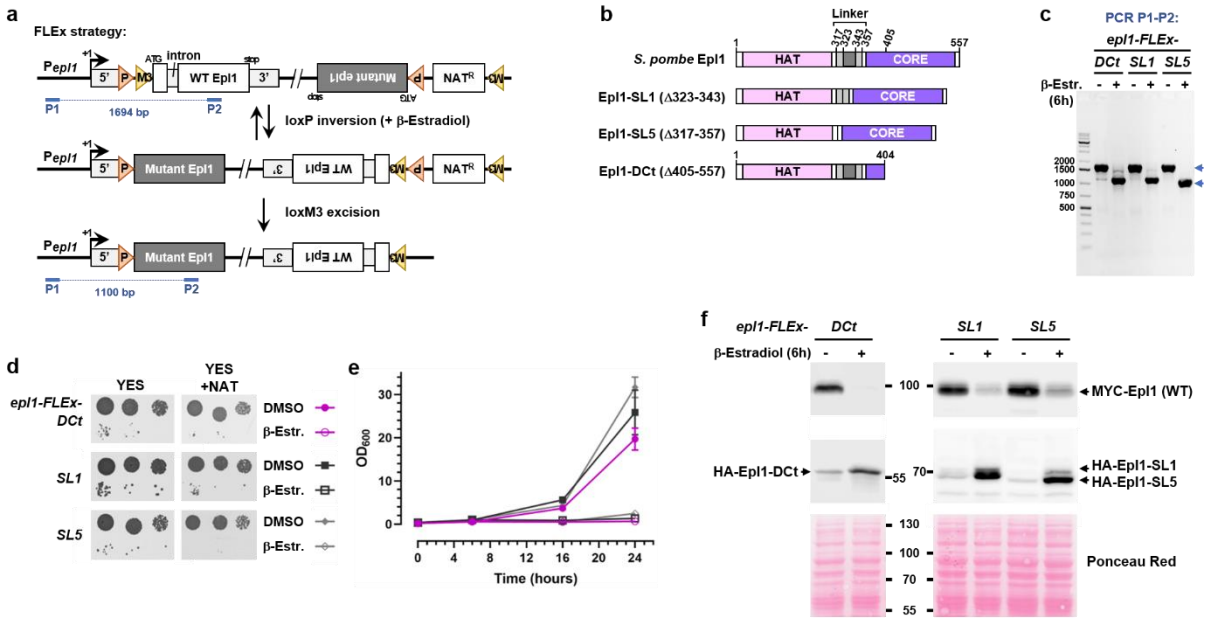

Figure 4 | A long Epl1 linker is essential for *S. pombe* viability. a, Illustration of the FLEx strategy to conditionally replace the WT *epl1*+ gene by an *epl1* mutant allele at the endogenous locus. Strains constitutively expressing a β-estradiol-inducible Cre-EBD78 carry incompatible loxP (red arrowhead) and loxM3 sites (yellow arrowhead) inserted immediately upstream of the *epl1*+ start codon, as well as the mutant *epl1* cDNA in antisense orientation, downstream of *epl1*+, along with loxP and loxM3 sites and a selection cassette. **b**, Illustration of *S. pombe* Epl1 linker mutants. The *epl1-SL1*, *-SL5*, and *-DCt* alleles have seamless deletions of residues 323-343, 317-357, and 405-557 of Epl1. **c**, PCR analysis using P1-P2 primers of genomic DNA extracted from liquid cultures of *epl1-FLEx-DCt*, *epl1-FLEx-SL1*, and *epl1-FLEx-SL5* strains, either treated with β-estradiol for 6 hours (+) or left untreated (-). Shown is a gel representative of two independent experiments. Shown are molecular weight markers in base pairs. **d-e**, Effect of Epl1 mutants on *S. pombe* proliferation and colony formation following treatment with either DMSO or β-estradiol as indicated. Each value represents average measurements from four independent replicates with the SD (n = 4). **f**, Western blot analysis of wild-type (WT) MYC-tagged Epl1 and mutant HA-tagged Epl1 in exponentially growing *S. pombe epl1-FLEx* mutants, grown and treated as in **c**. Ponceau red staining were used as a control for equal loading between lanes. Data are representative of four independent experiments. Shown are molecular weight markers in kiloDaltons. Source data for **c** and **f** are provided as a Source Data File.

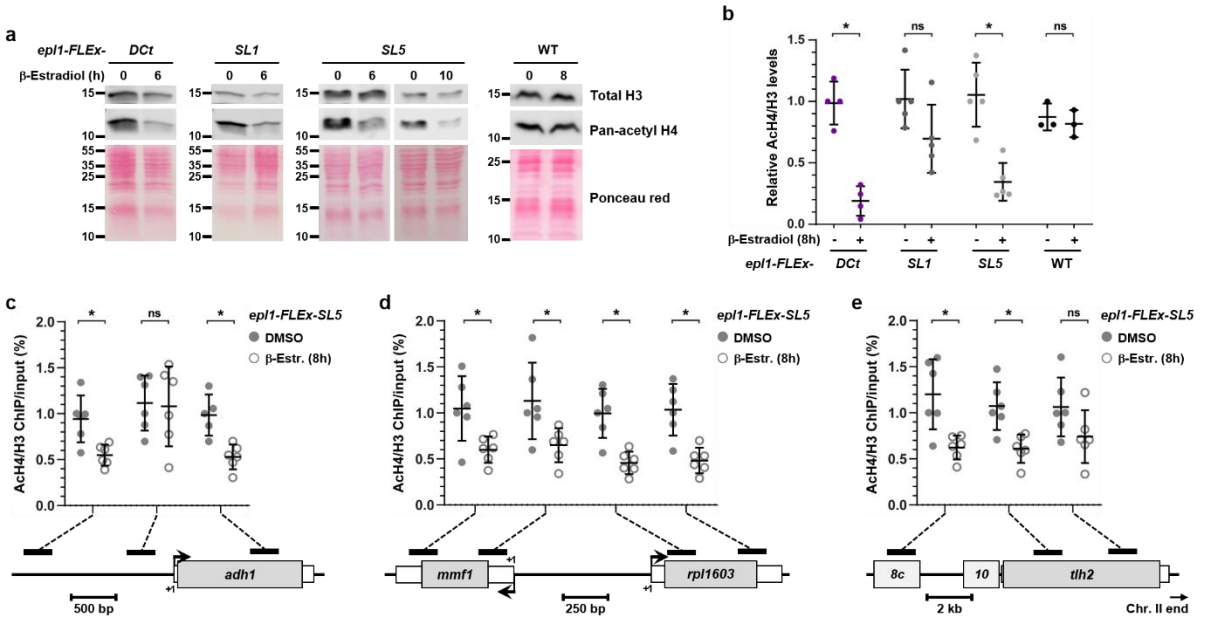

Figure 5 | The long Epl1 linker is important for NuA4 long-range activity. a, Western blot analysis of acetylated histone H4 levels in total protein extracts from exponentially growing WT control strains and *epl1-FLEx-DCt*, *epl1-FLEx-SL1*, and *epl1-FLEx-SL5* mutant strains, treated either with β-estradiol or DMSO for various time points, as indicated. An anti-H3 antibody and Ponceau red staining were used as controls for equal loading between lanes. Shown are molecular weight markers in kiloDaltons. Data are representative of three (WT), four (*epl1-FLEx-DCt*), or five (*epl1-FLEx-SL1* and *-SL5*) independent experiments, which signal intensity quantifications are shown in **b**. Acetyl-H4 levels were normalized to total H3. Data points from four independent experiments are plotted individually on the graph and overlaid with the mean and SD (*n* = 4). **c-e**, ChIP-qPCR analysis of acetyl-H4 and total H3 occupancy in chromatin extracts from *epl1-FLEx-SL5* strains treated either with β-estradiol or DMSO for 8 hours, over the upstream intergenic, promoter, and coding regions of the *adh1* gene (**c**), the coding regions of the *mmf1* and *rpl1603* genes (**d**), and the subtelomeric region of chromosome II right arm (**e**). The latter only contains silenced genetic elements, including the repressed *tlh2* gene and the *SPBCPT2R1.10* and *SPBCPT2R1.08c* pseudogenes.. Black bars represent the amplicons analyzed by qPCR and are shown on schematic illustrations of each locus, with a scale of the corresponding genomic distance. Ratios of anti-acetyl-H4 ChIP to input (IP/IN) were normalized to anti-H3 ChIP/IN ratios, from six independent experiments, which are shown as individual points (*n* = 6) overlaid with the mean and SD. **b-e**, Statistical significance was determined by two-way ANOVA followed by Šídák's multiple comparison tests (*n* = 4 in **b**; *n* = 6 in **c-e**); *P ≤ 0.05; ns: not significant. Source data for **a** are provided as a Source Data File. A detailed report of the statistical analyses is provided as Extended Data Table 4.

References:

1 Allard, S. *et al.* NuA4, an essential transcription adaptor/histone H4 acetyltransferase complex containing Esa1p and the ATM-related cofactor Tra1p. *Embo J* **18**, 5108-5119 (1999).

2 Clarke, A. S., Lowell, J. E., Jacobson, S. J. & Pillus, L. Esa1p is an essential histone acetyltransferase required for cell cycle progression. *Molecular and cellular biology* **19**, 2515-2526 (1999).

3 Doyon, Y. & Cote, J. The highly conserved and multifunctional NuA4 HAT complex. *Curr Opin Genet Dev* **14**, 147-154 (2004).

4 Bird, A. W. *et al.* Acetylation of histone H4 by Esa1 is required for DNA double-strand break repair. *Nature* **419**, 411-415 (2002).

5 Berndsen, C. E. *et al.* Nucleosome recognition by the Piccolo NuA4 histone acetyltransferase complex. *Biochemistry* **46**, 2091-2099, doi:10.1021/bi602366n (2007).

6 Xu, P. *et al.* The NuA4 Core Complex Acetylates Nucleosomal Histone H4 through a Double Recognition Mechanism. *Mol Cell* **63**, 965-975 (2016).

7 Reid, J. L., Iyer, V. R., Brown, P. O. & Struhl, K. Coordinate regulation of yeast ribosomal protein genes is associated with targeted recruitment of Esa1 histone acetylase. *Mol Cell* **6**, 1297-1307, (2000).

8 Vignali, M., Steger, D. J., Neely, K. E. & Workman, J. L. Distribution of acetylated histones resulting from Gal4-VP16 recruitment of SAGA and NuA4 complexes. *Embo J* **19**, 2629-2640 (2000).

9 Boudreault, A. A. *et al.* Yeast enhancer of polycomb defines global Esa1-dependent acetylation of chromatin. *Genes Dev* **17**, 1415-1428, (2003).

10 Auger, A. *et al.* Eaf1 is the platform for NuA4 molecular assembly that evolutionarily links chromatin acetylation to ATP-dependent exchange of histone H2A variants. *Molecular and cellular biology* **28**, 2257-2270, (2008).

11 Wang, X., Ahmad, S., Zhang, Z., Cote, J. & Cai, G. Architecture of the Saccharomyces cerevisiae NuA4/TIP60 complex. *Nat Commun* **9**, 1147, (2018).

12 Rossetto, D. *et al.* Eaf5/7/3 form a functionally independent NuA4 submodule linked to RNA polymerase II-coupled nucleosome recycling. *EMBO J* **33**, 1397-1415, (2014).

13 Brown, C. E. *et al.* Recruitment of HAT complexes by direct activator interactions with the ATM-related Tra1 subunit. *Science* **292**, 2333-2337. (2001).

14 Knutson, B. A. & Hahn, S. Domains of Tra1 important for activator recruitment and transcription coactivator functions of SAGA and NuA4 complexes. *Molecular and cellular biology* **31**, 818-831, (2011).

15 Grant, P. A., Schieltz, D., Pray-Grant, M. G., Yates, J. R., 3rd & Workman, J. L. The ATM-related cofactor Tra1 is a component of the purified SAGA complex. *Mol Cell* **2**, 863-867, (1998).

16 Venters, B. J. *et al.* A comprehensive genomic binding map of gene and chromatin regulatory proteins in Saccharomyces. *Mol Cell* **41**, 480-492, (2011).

17 Bruzzone, M. J., Grunberg, S., Kubik, S., Zentner, G. E. & Shore, D. Distinct patterns of histone acetyltransferase and Mediator deployment at yeast protein-coding genes. *Genes Dev* **32**, 1252-1265, (2018).

18 Lenstra, T. L. *et al.* The specificity and topology of chromatin interaction pathways in yeast. *Mol Cell* **42**, 536-549, (2011).

19 Li, B. *et al.* Preferential occupancy of histone variant H2AZ at inactive promoters influences local histone modifications and chromatin remodeling. *Proceedings of the National Academy of Sciences of the United States of America* **102**, 18385-18390, (2005).
20 Zhang, H., Roberts, D. N. & Cairns, B. R. Genome-wide dynamics of Htz1, a histone H2A variant that poises repressed/basal promoters for activation through histone loss. *Cell* **123**, 219-231, (2005).
21 Yan, Z. *et al.* Structure of the rabbit ryanodine receptor RyR1 at near-atomic resolution. *Nature* **517**, 50-55, (2015).
22 Mitchell, L. *et al.* Functional dissection of the NuA4 histone acetyltransferase reveals its role as a genetic hub and that Eaf1 is essential for complex integrity. *Molecular and cellular biology* **28**, 2244-2256, (2008).
23 Setiaputra, D. *et al.* Molecular Architecture of the Essential Yeast Histone Acetyltransferase Complex NuA4 Redefines Its Multimodularity. *Molecular and cellular biology* **38**, (2018).
24 Papai, G. *et al.* Structure of SAGA and mechanism of TBP deposition on gene promoters. *Nature* **577**, 711-716, (2020).
25 Clark, M. D. *et al.* Structural insights into the assembly of the histone deacetylase-associated Sin3L/Rpd3L corepressor complex. *Proceedings of the National Academy of Sciences of the United States of America* **112**, E3669-3678, (2015).
26 Cai, Y. *et al.* Identification of new subunits of the multiprotein mammalian TRRAP/TIP60-containing histone acetyltransferase complex. *J Biol Chem* **278**, 42733-42736, (2003).
27 Elias-Villalobos, A., Toullec, D., Faux, C., Seveno, M. & Helmlinger, D. Chaperone-mediated ordered assembly of the SAGA and NuA4 transcription co-activator complexes in yeast. *Nat Commun* **10**, 5237, (2019).
28 Knoll, K. R. *et al.* The nuclear actin-containing Arp8 module is a linker DNA sensor driving INO80 chromatin remodeling. *Nat Struct Mol Biol* **25**, 823-832, (2018).
29 Wang, H. *et al.* Structure of the transcription coactivator SAGA. *Nature* **577**, 717-720, (2020).
30 Reeves, W. M. & Hahn, S. Targets of the Gal4 transcription activator in functional transcription complexes. *Molecular and cellular biology* **25**, 9092-9102, (2005).
31 Galarneau, L. *et al.* Multiple links between the NuA4 histone acetyltransferase complex and epigenetic control of transcription. *Mol Cell* **5**, 927-937, (2000).
32 Searle, N. E., Torres-Machorro, A. L. & Pillus, L. Chromatin Regulation by the NuA4 Acetyltransferase Complex Is Mediated by Essential Interactions Between Enhancer of Polycomb (Epl1) and Esa1. *Genetics* **205**, 1125-1137, (2017).
33 Hayles, J. *et al.* A genome-wide resource of cell cycle and cell shape genes of fission yeast. *Open Biol* **3**, 130053, (2013).
34 Schnutgen, F. *et al.* A directional strategy for monitoring Cre-mediated recombination at the cellular level in the mouse. *Nat Biotechnol* **21**, 562-565, (2003).
35 Nourani, A., Utley, R. T., Allard, S. & Cote, J. Recruitment of the NuA4 complex poises the PHO5 promoter for chromatin remodeling and activation. *EMBO J* **23**, 2597-2607, (2004).
36 Lantermann, A. B. *et al.* Schizosaccharomyces pombe genome-wide nucleosome mapping reveals positioning mechanisms distinct from those of Saccharomyces cerevisiae. *Nat Struct Mol Biol* **17**, 251-257, doi:10.1038/nsmb.1741 (2010).
37 Moyle-Heyrman, G. *et al.* Chemical map of Schizosaccharomyces pombe reveals species-specific features in nucleosome positioning. *Proceedings of the National Academy of Sciences of the United States of America* **110**, 20158-20163, (2013).

38 Kastner, B. *et al.* GraFix: sample preparation for single-particle electron cryomicroscopy. *Nat Methods* **5**, 53-55, (2008).
39 Schindelin, J. *et al.* Fiji: an open-source platform for biological-image analysis. *Nat Methods* **9**, 676-682, (2012).
40 Toullec, D. *et al.* The Hsp90 cochaperone TTT promotes cotranslational maturation of PIKKs prior to complex assembly. *Cell Rep* **37**, 109867, (2021).
41 Mastronarde, D. N. Automated electron microscope tomography using robust prediction of specimen movements. *J Struct Biol* **152**, 36-51, (2005).
42 Tegunov, D. & Cramer, P. Real-time cryo-electron microscopy data preprocessing with Warp. *Nat Methods* **16**, 1146-1152, (2019).
43 Zivanov, J. *et al.* New tools for automated high-resolution cryo-EM structure determination in RELION-3. *Elife* **7**, (2018).
44 Punjani, A., Rubinstein, J. L., Fleet, D. J. & Brubaker, M. A. cryoSPARC: algorithms for rapid unsupervised cryo-EM structure determination. *Nat Methods* **14**, 290-296, (2017).
45 Kucukelbir, A., Sigworth, F. J. & Tagare, H. D. Quantifying the local resolution of cryo-EM density maps. *Nat Methods* **11**, 63-65, (2014).
46 Zhong, E. D., Bepler, T., Berger, B. & Davis, J. H. CryoDRGN: reconstruction of heterogeneous cryo-EM structures using neural networks. *Nat Methods* **18**, 176-185, (2021).
47 Yang, J. & Zhang, Y. I-TASSER server: new development for protein structure and function predictions. *Nucleic Acids Res* **43**, W174-181, (2015).
48 Emsley, P., Lohkamp, B., Scott, W. G. & Cowtan, K. Features and development of Coot. *Acta Crystallogr D Biol Crystallogr* **66**, 486-501, (2010).
49 Kallberg, M. *et al.* Template-based protein structure modeling using the RaptorX web server. *Nat Protoc* **7**, 1511-1522, (2012).
50 Buchan, D. W., Minneci, F., Nugent, T. C., Bryson, K. & Jones, D. T. Scalable web services for the PSIPRED Protein Analysis Workbench. *Nucleic Acids Res* **41**, W349-357, (2013).
51 Terwilliger, T. C. Rapid model building of alpha-helices in electron-density maps. *Acta Crystallogr D Biol Crystallogr* **66**, 268-275, (2010).
52 Goddard, T. D., Huang, C. C. & Ferrin, T. E. Visualizing density maps with UCSF Chimera. *J Struct Biol* **157**, 281-287, (2007).
53 Goddard, T. D. *et al.* UCSF ChimeraX: Meeting modern challenges in visualization and analysis. *Protein Sci* **27**, 14-25, (2018).

Methods:

Purification of NuA4

A strain of the budding yeast *Komagataella phaffii* (also known as *Pichia pastoris*) with the 38-amino-acid streptavidin-binding peptide (SBP) affinity tag fused to the C-terminus of the endogenous Eaf1 subunit was produced following standard yeast molecular biology techniques. Two liters of yeast cells were grown at 24°C with glycerol as carbon source and harvested when $OD_{600\ nm}$ reached 16-18. Cells were washed in ice-cold water and then treated with 10 mM DTT in 1.1 M Sorbitol. The cell wall was digested by addition of lyticase at 30°C and spheroplasts were pelleted at 5,500 g for 24 min. All further steps were performed at 0 to 4°C. Protease inhibitors were added to all buffers. Spheroplasts were washed twice in 1.4 M Sorbitol and were then disrupted by suspension in a hypotonic buffer (15-18% Ficoll

400, 0.6 mM $MgCl_2$, 20 mM K-phosphate buffer pH 6.6) using a ULTRA-TURRAX disperser. Sucrose (0.1 M) and $MgCl_2$ (5 mM) were then added. Nuclei (and some debris) were pelleted at 34,000 g for 38 min, re-suspended in a wash buffer (0.6 M Sucrose, 8% PVP, 1 mM $MgCl_2$, 20 mM phosphate buffer pH 6.6) and pelleted again at 34,000 g for 50 min. Nuclei were re-suspended in low ionic extraction buffer (40 mM HEPES pH 8.0, 20% sucrose, 8 mM $MgCl_2$, 5-6 mM DTT) with 30 strokes using a tight pestle in a dounce homogenizer. Very few molecules of NuA4 are liberated under the low ionic conditions leaving time for protease inhibitors to bind their targets before NuA4 is extracted. After 20 minutes of incubation, 300 mM NaCl, 0.25 mM $CaCl_2$ and 150 ul of alpha-Amylase solution (MegaZyme) were added. Following another 30 minutes of incubation, debris were precipitated at 34,000 g for 40 min. The supernatant was collected and 1.4 % PEG 20,000 as well as additional 5 mM $MgCl_2$ were added in order to precipitate some remaining organelles and membrane parts by a short centrifugation (33,000 g for 10 min). The PEG 20,000 concentration was then increased to 5.8% and NUA4 precipitated in a second short centrifugation step. The pellet was re-suspended in a minimal volume and avidin was added to block endogenously biotinylated proteins. The suspension was incubated with streptavidin beads for 5 h in buffer A (20 mM HEPES pH 8.0, 250 mM Sodium Chloride, 10% sucrose, 2 mM $MgCl_2$, 2 mM DTT) washed 5 times with buffer A supplemented with 0.05% Tween-20 and finally eluted with buffer A containing 10 mM biotin. The eluate was concentrated with Millipore Amicon-Ultra (50 kDa cut-off) and loaded on a sucrose gradient generated by a Gradient Master 108 (BioComp) from a light solution (10% sucrose, 20 mM HEPES pH 8.0, 150 mM Potassium acetate, 2 mM TCEP, 5 mM $MgCl_2$, 0.0045% Dodecyl-maltoside) and a heavy solution (30% sucrose instead of 10%) that contained 0.1% Glutaraldehyde[38]. Following centrifugation in rotor SW60 (42,000 rpm for 14 h) the gradient was fractionated by puncturing the bottom of the tube with a needle. Glutaraldehyde was quenched by addition of 75 mM ammonium acetate. Peak fractions were concentrated (Millipore Amicon-Ultra) and dialyzed against a buffer containing 20mM Hepes pH 8, 150mM Potassium acetate, 5mM Magnesium acetate, 2mM TCEP, 5mM Ammonium acetate, 0.0025% Dodecyl-maltoside. The quality of the sample and its concentration after dialysis was estimated by electron microscopy of negatively stained samples.

Yeast procedures and growth conditions

Standard culture media and genetic manipulations were used. *S. cerevisiae* strains were grown in YPD at 30˚C to mid-log phase (~$1x10^7$ cells/ml). *S. pombe* strains were grown in either rich (YES) or minimal (EMM) media at 32˚C to mid-log phase (~$0.5x10^7$ cells/ml). Proliferation assays were performed by inoculating single colonies in liquid media and measuring the optical density at 595 nm at different time points and by spotting ten-fold serial dilutions of liquid cultures on rich medium and incubated for 3 days at 32°C. For longer time course, cultures were diluted to keep cells in constant exponential growth. For CreER-loxP-mediated recombination, cells were treated with either 1 µM β-estradiol (E2758, Sigma) or DMSO alone for various time points, as indicated.

Strain construction

All *S. pombe* and *S. cerevisiae* strains used are listed in Extended Data Table 2 and were constructed by standard procedures, using either yeast transformation or genetic crosses. Strains with truncations and C-terminally epitope-tagged proteins were constructed by PCR-based gene targeting of the respective open reading frame (ORF) with kanMX6, amplified from pFA6a backbone plasmids. Strains with N-terminally epitope-tagged proteins and internal deletions were constructed using CRISPR-Cas9-mediated genome editing. DNA fragments used for homologous recombination were generated by PCR, Gibson assembly cloning (kit E2611L, New England Biolabs), or gene synthesis. Transformants were screened for correct integration by PCR and, when appropriate, verified by Sanger sequencing or Western blotting. For each transformation, 2-4 individual clones were purified and analyzed. For tetrad analyses in both *S. cerevisiae* and *S. pombe* (Extended Data Fig. 10 and 11), mutations were introduced in diploid strains to generate heterozygotes, which were then sporulated to analyze growth phenotypes. At least 20 distinct meiotic events were analyzed for growth and allele segregation by replica plating and PCR. The four progenies from each tetrad are labelled A-D (Extended Data Fig. 11b).

Construction of S. cerevisiae *epl1* linker mutants

To construct seamless deletions of the linker region from endogenous *S. cerevisiae* Epl1, and avoid possible issues with the genetic manipulation of an essential gene, we took advantage of the ability of *sds3*Δ deletion mutants to suppress the loss of viability observed in NuA4 HAT mutants, including *epl1*Δ[32]. In this background, we obtained an *epl1-SL1* allele, which removes residues K395 to V501, and an *epl1-SL5* allele, in which Epl1 lacks residues I401 to H487. The *sds3*Δ *epl1-SL1* and *sds3*Δ *epl1-SL5* double mutants were then backcrossed to a wild-type (WT) strain to segregate each mutant allele independently.

Construction of endogenous conditional mutants in *S. pombe*

Using the FLEx strategy originally developed in mice [34], we constructed *S. pombe* strains in which we can conditionally replace the WT *epl1*+ allele with a mutant copy of *epl1* at its endogenous locus, thereby leaving all 5' *cis*-regulatory elements intact. Specifically, we obtained two Epl1-FLEx mutants, *epl1-SL1-FLEx* and *epl1-SL5-FLEx*, which have seamless deletions of residues V323-to-A343 and K317-to-P357, respectively. We also designed an *epl1-DCt-FLEx* allele, in which Epl1 is conditionally replaced by the same C-ter truncation mutant analyzed in heterozygous diploids (Y405-to-stop) (Fig. 4a).

Generation of *P. pastoris epl1* linker mutants

We used the NEBuilder enzyme mixture (NEB) to assemble seamlessly together into a linearized pUC19 backbone these DNA fragments: 1000 base-pairs upstream in the yeast genome to the position of the deletion in the linker; yeast genome sequence from the deletion till the end of Epl1; affinity tag sequence with a stop codon followed by the AOX gene transcription termination sequence; Zeocin selection marker; 1000 base-pairs in the yeast

genome downstream to Epl1. PCR was used to amplify the assembled DNA. Pichia pastoris X33 wild type cells were transformed with 180ug of the PCR product by electroporation.

Histone acetyl transferase activity

The activity test reactions were carried out in 20 mM HEPES (pH 7.5), 50 mM NaCl, 50 µM acetyl-CoA, 0.1 mg/ml BSA, 2 mM MgCl2, 1 mM DTT, 0.0025% Dodecyl-maltoside, 10% (v/v) Glycerol and 1 µM Nucleosome. The reactions were initiated by adding 10 nM of NuA4, Piccolo or NuA4-SL1/3/5. After an incubation on ice for 10 min the reactions were stopped by adding SDS loading buffer and heating at 95°C for 3 min. Proteins were then resolved by 15% SDS-PAGE that was followed by a western blot with a primary antibody against acetylated-lysine (Cell Signaling Technology Cat. No. 9441S).

Protein extraction and Western blotting

Ten to twenty-fine mL cultures of exponentially growing cells were homogenized by glass bead-beating in a FastPrep (MP Biomedicals). Proteins extracted using either standard lysis buffer (WEB: 40 mM HEPES-NaOH pH 7.4, 350 mM NaCl, 0.1% NP40, and 10% glycerol) or trichloroacetic acid (TCA) precipitation. WEB was supplemented with protease inhibitors, including cOmplete EDTA-free cocktails tablets (04693132001, Roche), 1 mM PMSF (P7626, Sigma), 1 µg/ml bestatin (B8385, Sigma), and 1 µg/ml pepstatin A (P5318, Sigma). Western blotting was performed using the anti-pan-acetyl H4 (rabbit polyclonal, 06-866, Sigma), anti-H3 (rabbit polyclonal, ab1791, Abcam), anti-HA (16B12), or anti-Myc (9E11) antibodies. Protein concentrations were measured by the Bradford method and used to load equal amounts of proteins across samples. Ponceau red was used to normalize for total protein levels across samples. Quantification of signal intensity was performed on digitally acquired images of the chemiluminescence signal, using an Odyssey XF imaging system (LI-COR), and analyzed with ImageJ[39].

Statistical analysis

All statistical tests were performed using GraphPad Prism (version 9.2.0). *t* tests were used when comparing two means. Oneway and two-way analyses of variance (ANOVA) were performed for comparing more than two means, across one (for example “genotype”) and two variables (for example “genotype” as a between-subject factor and “treatment” as a within-subject factor), respectively. One-way and two-way ANOVAs were followed by Tukey and Bonferroni post-hoc pairwise comparisons, respectively. A significance level (α) of 0.05 was used a priori for all statistical tests, except otherwise indicated. Comparisons that are statistically significant ($P \leq 0.05$) are marked with one asterisk. Statistical details of experiments can be found in the figure legends, including the statistical tests used, the minimum value of biological replicates n shown (n = isogenic clones of each strain), and a description of the center and dispersion statistics. Quantitative values are represented as individual values (n) overlaid with the mean (black bar) and standard deviation (SD).

Chromatin immunoprecipitation

ChIP experiments were performed as previously described[40]. Briefly, cell cultures were

crosslinked in 1% formaldehyde for 30 min. Cells were then lysed using a FastPrep (MP Biomedicals) and the chromatin fraction was sheared to 200–300 bp fragments using a Bioruptor Pico sonicator (DIagenode) for 30 cycles (each 30 seconds on, 30 seconds off). For immunoprecipitation (IP), 3 µg of the anti-pan-acetyl H4 (rabbit polyclonal, 06-866, Sigma) and anti-H3 (rabbit polyclonal, ab1791, Abcam) were incubated overnight at 4°C with chromatin extracts and then coupled with 50 µl of protein-G-coupled magnetic beads (Dynabeads, Invitrogen) during 5h at 4°C. Purified input and IP DNA samples were analyzed by quantitative PCR using SYBR Green. Relative DNA quantities were calculated from the slope produced by standard curves for each primer pair, in each experiment. Standard curve slopes were comprised between -3.5 (90% efficiency) and -3.15 (110% efficiency), with an $r^2 > 0.9$. Both input and IP samples were diluted 50-fold for qPCR. Relative occupancy levels were determined by dividing the IP by the IN value (IP/IN) for each amplicon, correcting for the dilation factor of input and IP samples. All primer sequences are listed in Extended Data Table 3.

Cryo-EM sample preparation and data acquisition

Three µl of sample was applied onto a holey carbon grid (Quantifoil R2/2 300 mesh) rendered hydrophilic by a 90 s treatment in a Fischione 1070 plasma cleaner operating at 30% power with a gas mixture of 80% argon: 20% oxygen. The grid was blotted for 1 sec at blot force 8 and flash-frozen in liquid ethane using Vitrobot Mark IV (FEI) at 4˚C and 95-100% humidity. Images were acquired on a Cs-corrected Titan Krios (Thermo Fisher) microscope operating at 300 kV in nanoprobe mode using the serialEM software for automated data collection[41]. Movie frames were recorded either on a Gatan K2 Summit or on a Gatan K3 direct electron detector after a Quantum Ls 967 energy filter using a 20 eV slit width in zero-loss mode. Images were collected in super-resolution mode at a nominal magnification of 105,000x (K2 summit) or 81,000x (K3) which yielded a pixel size of 0.55 or 0.852 Å. For each image, 40 movie frames were recorded at a dose of 1.32 electrons per Å² per frame corresponding to a total dose of 52.8 e/Å^2, but only the last 38 frames were kept for further processing.

Image processing

WARP was used to perform the first pre-processing steps, aligning movie frames, dose-weighting, correct the beam-induced specimen motion and Contrast Transfer Function (CTF) estimation[42]. After visual inspection, images with poor CTF, showing particle aggregation or abundant ice contamination were discarded. Particle coordinates were determined using crYOLO (doi: https://doi.org/10.1101/356584). The datasets were analyzed in Relion 3.1[43] and cryoSPARC[44] according to standard protocols. Briefly, three rounds of reference free 2D classification of the individual particle images were performed in cryoSPARC to remove images corresponding to contaminating or damaged particles and ice contaminations. Four references (3-D models) were generated by the *ab initio* 3-D reconstruction program of cryoSPARC. These structures were then used as references for a 3D classification job in cryoSPARC, and particles corresponding to high resolution 3-D classes were selected and used for non-uniform refinement. We carried out a focused refinement of different part of NuA4 using the masked including upper lobes, the head of Tra1 and their junction or just the upper lobe. Global resolution estimates were determined using the FSC = 0.143 criterion after a gold-standard refinement.

Local resolutions were estimated with ResMap[45] and cryoSPARC. To analyze the heterogeneity in the cryo-EM map due to the presence of the flexible Piccolo module (MW: 144 kDa), we used the neural network-based cryoDRGN reconstruction to map the particles on 2 principal components[46]. For each WT and short linker mutant data set, we partitioned the latent space into twenty regions and a density map was generated from the center of each region. The maps were thresholded to a value that corresponds to the expected volume of NuA4 (MW: 1.030.447 Da), assuming an average protein density of 0.825 Da/A^3. Upon visual inspection, the maps were grouped into three classes according to the absence (class 1) or the presence of an additional mass disconnected (class 2) or connected (class 3) to the core of NuA4. To determine the low-resolution map of Piccolo, the density of the stable core-NuA4 was subtracted from the original images and the images were re-centered according to the expected position of Piccolo. A two-dimensional classification step was performed to assure the correct subtraction of the core of NuA4 and the presence of a residual density. *Ab-initio* reconstruction followed by 3D classification steps in cryoSPARC were used to reconstruct the map of Piccolo at 12 Å resolution. Heterogeneous 3D refinement of the dataset lowpass filtered to 1/6 $Å^{-1}$ produced a reconstruction at 11.5 Å resolution.

Model building

Homology models for Act1, Arp4 and the SANT domains of Eaf1 and Swc4 were generated using iTASSER[47] or Swiss-model and docked into the maps using the chimera docking tool. Eaf1, Swc4 and Epl1 where build de-novo using the Coot software[48]. To facilitate de-novo model building, the web service RaptorX[49] and PSIPRED[50] were used to predict secondary structure and disordered parts. A large proportion of the coulombic potential difference map (hereafter called density) associated to each side chain was clear and practically all densities in the core of NuA4 could be assigned with confidence. For Eaf1 residues 367-389 and Tra1 residues 4-300, 2019-2392 and 2969-3051, the local resolution of the structure did not allow us to place the side chain but was enough to place helices and trace the C-alpha backbone. The atomic model was refined in Phenix by real-space refinement with secondary structure restrains[51]. All display images were generated using UCSF Chimera[52] and ChimeraX[53].

Data Availability:

The cryo-EM maps have been deposited in the electron microscopy database (EMBD) under accession codes EMDB-15869 (NuA4 WT-overall), EMDB-15881 (NuA4 WT-core), EMDB-15896 (NuA4-SL1-overall), EMDB-15897 (NuA4-SL1-core), EMDB-14980 (NuA4-SL3-overall), EMDB-15066 (NuA4-SL3-core), EMDB-15070 (NuA4-SL3-tra1-tail) and EMDB-15067 (NuA4-SL3-tra1-ring). A composite map was also deposited for NuA4-SL3 (EMDB-14989). The model coordinates for core NuA4 derived from the SL3 composite map were deposited in the PDB database under the accession codes 7ZVW.

Extended Data figure legends

a

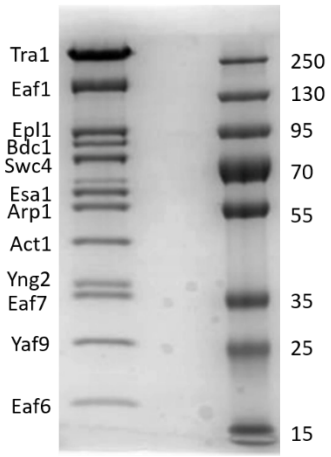

b

Accession	Description	# PSMs	# AAs	NSAF (PSM/ AA)	NSAF norm. to Tra1
C4QYV4	Tra1	5973	3825	1,6	1,0
C4R7G0	Eaf1	2304	1051	2,2	1,4
C4R6V1	Epl1-SL1	1087	703	1,5	1,0
C4R0G7	Swc4	1044	565	1,8	1,2
C4R4E2	Bdc1	909	568	1,6	1,0
Q9P4D1	Actin	896	376	2,4	1,5
C4QXM9	Arp4	754	468	1,6	1,0
C4R6T5	Tip60	738	464	1,6	1,0
C4R7P5	Yaf9	617	219	2,8	1,8
C4R522	Importin α	448	548	0,8	0,5
C4R205	Eaf7	311	237	1,3	0,8
C4R0B2	Yng2	263	261	1,0	0,6
C4QXE0	Eaf6	233	141	1,7	1,1
P04264	Type II keratin	217	643	0,3	0,2
C4R887	ATPase	202	645	0,3	0,2
C4QXW1	Acetyl-CoA carboxylase	178	2215	0,1	0,1

c

P. pastoris	*S. cerevisiae*	*S. pombe*
Tra1	Tra1	Tra2
Eaf1	Eaf1	Vid21
Swc4	Swc4	Swc4
Act1	Act1	Act1
Arp4	Arp4	Alp5
Yaf9	Yaf9	Yaf9
Esa1	Esa1	Mst1
Epl1	Epl1	Epl1
Yng2	Yng2	Png1
Eaf6	Eaf6	Eaf6
Bdc1		Bdc1
Eaf7	Eaf7	Eaf7
	Eaf5	
	Eaf3	Alp13

Extended Data Figure 1 | Subunit characterization of the purified *P. pastoris* NuA4 complex. **a**, Colloidal coomassie blue stained SDS-PAGE analysis of the *P. pastoris* NuA4 complex purified from a SBP-tagged Eaf1 subunit. Bdc1 is the bromodomain protein homologous to human BRD8 and *S. pombe* Bdc1. **b**, Proteomic analysis of the purified NuA4 complexes. For each identified protein subunit, the table shows the peptide spectrum matches (PSM) counts, the number of residues, the PSM values normalized by subunit length (NSAFs) and the NSAF value normalized to Tra1. For each protein values were averaged over 3 experiments. **c**, Subunit names and composition of the NuA4 complexes purified from the *P. pastoris*, *S. cerevisiae* and *S. pombe* yeast species.

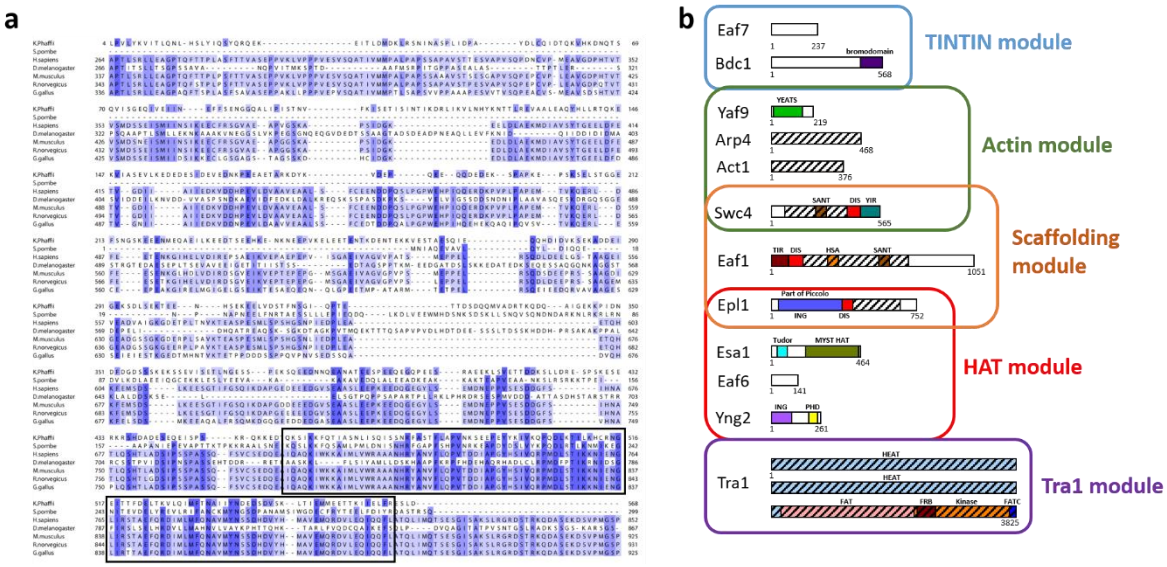

Extended Data Figure 2 | Subunit and domain organization of the yeast NuA4 complex.
a, Multiple sequence alignment between the bromodomain-containing subunit associated with purified *P. pastoris* NuA4, the *S. pombe* Bcd1 subunit and BDR8 subunits from human, drosophila, mouse, rat and chicken. The conserved C-terminal bromodomain is boxed. **b**, NuA4 subunits are organized into an enzymatic HAT (or Piccolo) module, an activator binding Tra1 module, an actin module and a TINTIN module interconnected by a Scaffolding module. Protein domains are abbreviated as follows: YEATS (Yaf9, ENL, AF9, Taf14, Sas5 domain), SANT (Swi3, Ada2, N-Cor, TFIIIB domain), DIS (disordered region), YIR (Yaf9 interacting region), TIR (Tra1 Interacting region), HSA (Helicase SANT associated), MYST HAT (MOZ, Ybf2/Sas3, Sas2, Tip60 family of Histone Acetyl Transferase), ING (domain found in the inhibitor of Growth family of proteins), PHD (plant homeodomain), HEAT (α-helical repeats found in Huntingtin, Elongation factor 3, Protein phosphatase 2A and Tor kinase), FAT (four helix bundle found in FRAP, ATM and TRRAP), FRB (N-terminal FKBP12-Rapamycin Binding kinase domain), FATC (kinase domain important for assembly).

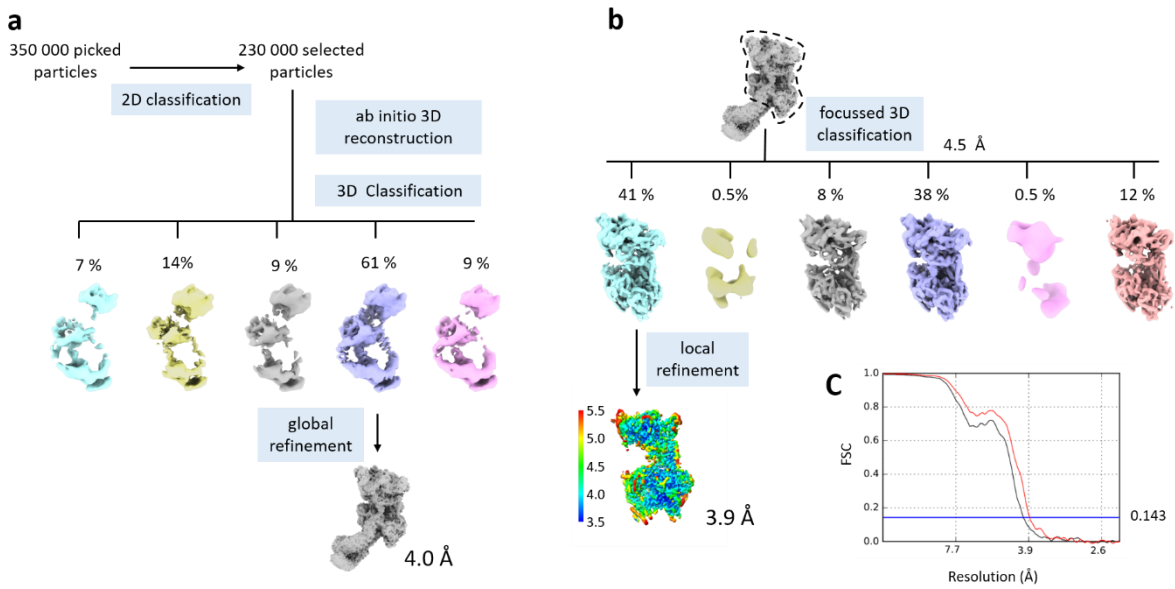

Extended Data Figure 3 | Cryo-EM data analysis strategy and resolution assessment of the cryo-EM structure of WT *P. pastoris* NuA4.

a, Image processing strategy used to obtain a map of the full *P. pastoris* NuA4 complex. **b**, Refinement steps of the volume masked as shown by the dotted contour. The map colored in rainbow spectrum represent the local resolution of the reconstruction of the masked volume. **c**, Fourier Shell Correlation (FSC) curves are depicted as a function of resolution in Å for the entire NuA4 complex (black) and the masked volume (red).

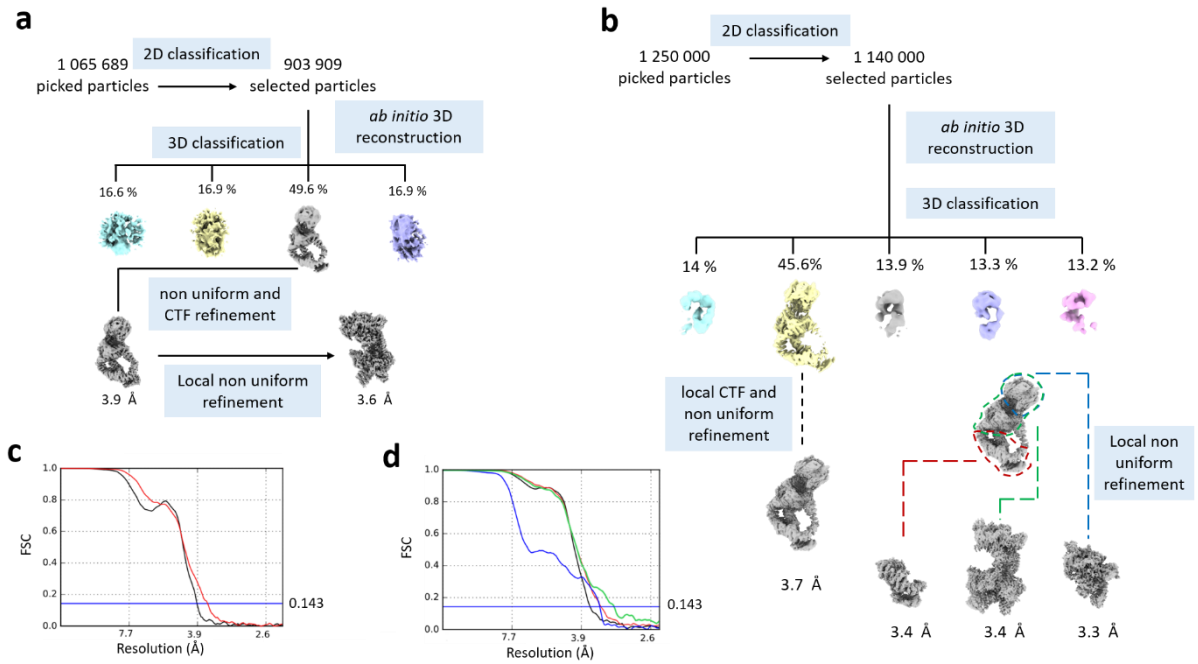

Extended Data Figure 4 | Cryo-EM data analysis and resolution assessment of the cryo-EM structures of Epl1-SL1 and Epl1-SL3 NuA4 mutants.

a, Image processing used to obtain the maps of the NuA4 complex containing the Epl1-SL1 mutation and of the masked lobe. **b**, Image processing used to obtain the maps of the NuA4 complex containing the Epl1-SL3 mutation and of three masked domains depicted by dotted lines. **c**, Fourier Shell Correlation (FSC) curves are depicted as a function of resolution in Å for the entire NuA4 Epl1-SL1 complex (black) and the masked areas (red). **d**, Fourier Shell Correlation (FSC) curves are depicted as a function of resolution in Å for the entire NuA4 Epl1-SL3 complex (black) and the three masked areas (red, green and blue).

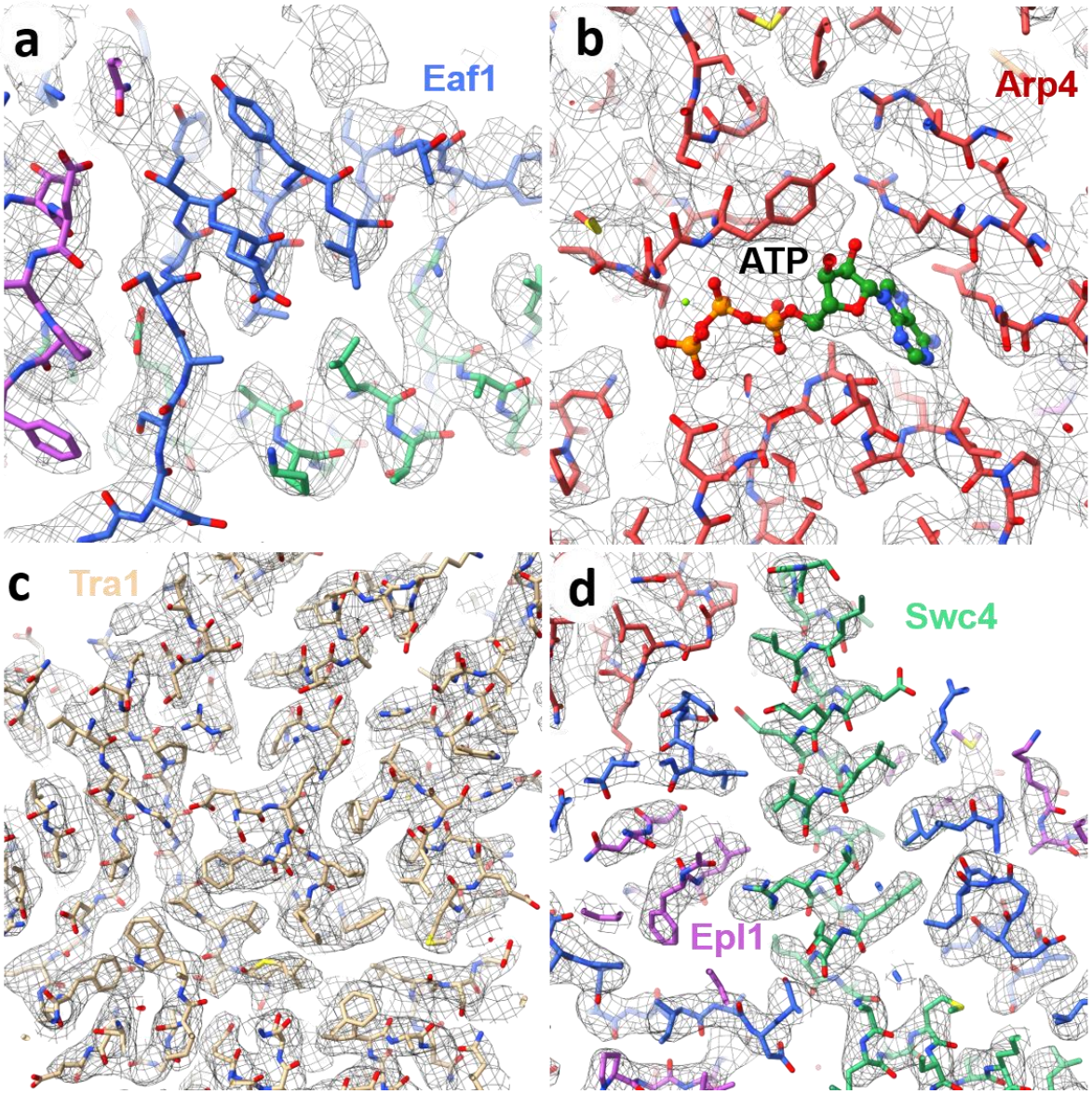

Extended Data Figure 5 | High resolution structure of the yeast NuA4 complex.
Representative regions illustrating the quality of the cryo-EM map and the high-resolution structural features. Cryo-EM map and atomic model showing that side chains are clearly identified. **a,** Part of the Eaf1 subunit **b,** ATP molecule bound in the Arp4 active site. **c**, Part of the Tra1 subunit. **d**, Interaction network between the Swc4, Epl1 and Eaf1 subunits in the neck region.

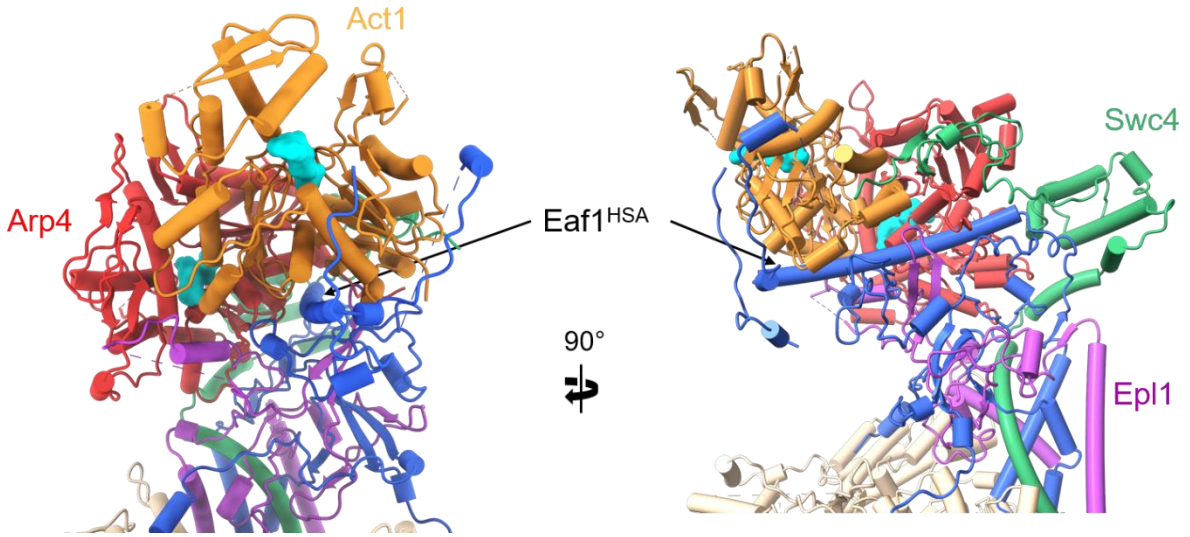

Extended Data Figure 6 | Unique environment of the Act1/Arp4/Eaf1^{HSA} module. The Act1 and Arp4 subunits interact with one side of the Eaf1 HSA helix while the opposite face is sheltered by structural motifs from Epl1 and Swc4 subunits. ATP molecules (cyan) were found associated with the active sites of Act1 and Arp4.

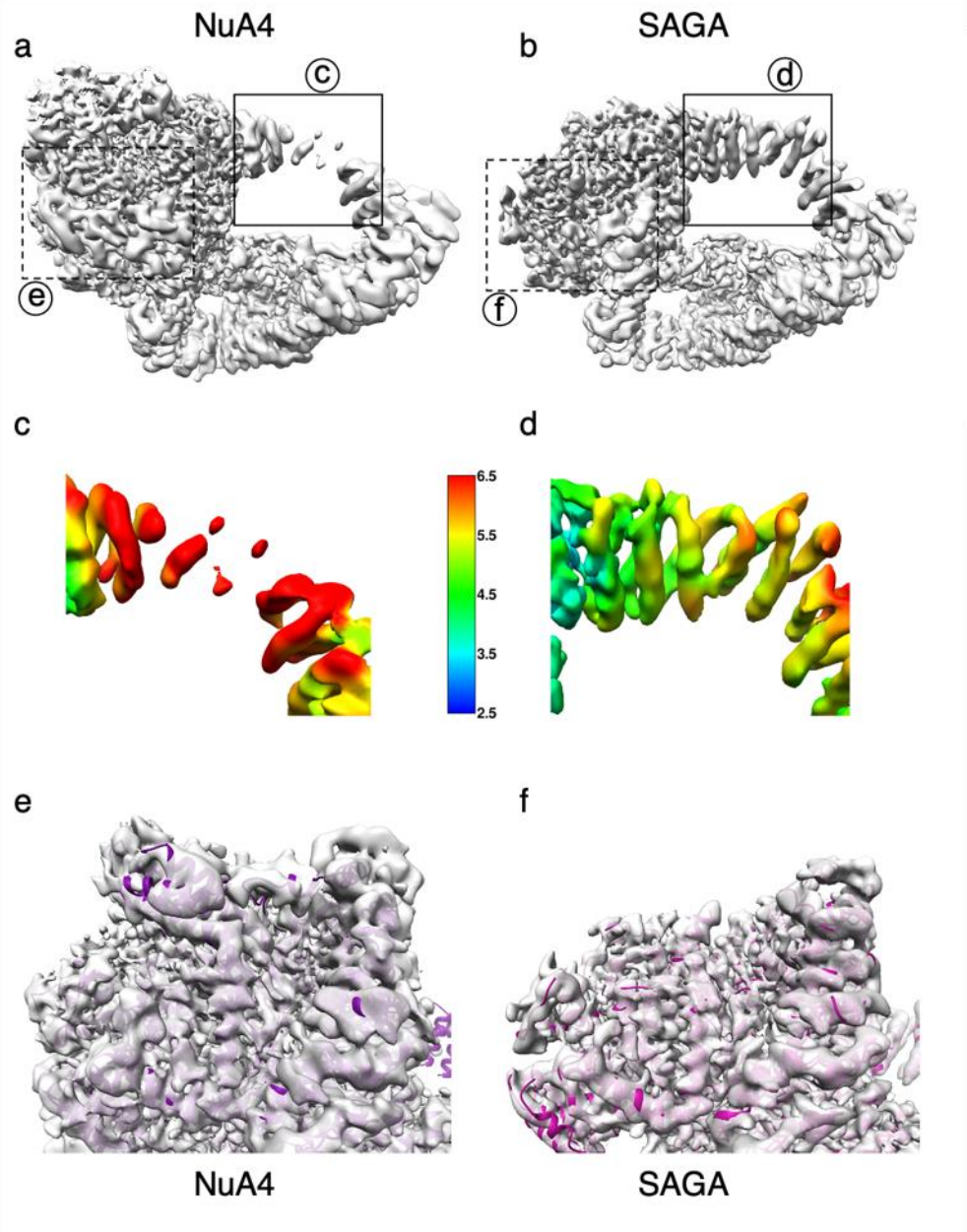

Extended Data Figure 7 | Mobility of Tra1 domains in NuA4 and SAGA.
Cryo-EM maps of NuA4 Tra1 **(a)** and of SAGA Tra1 **(b)**. The Tra1 ring solenoid and the FRB/LBE domains of the Tra1 pseudo kinase are labelled HEAT and FRB/LBE, respectively. Local resolution map of the Tra1 HEAT domain in NuA4 **(c)** and in SAGA **(d)**. The colored bar indicates the local resolution in Å. Cryo-EM maps of NuA4 Tra1 **(e)** and of SAGA Tra1 **(f)** enlarged and oriented to visualize the FRB/LBE domain of the pseudokinase.

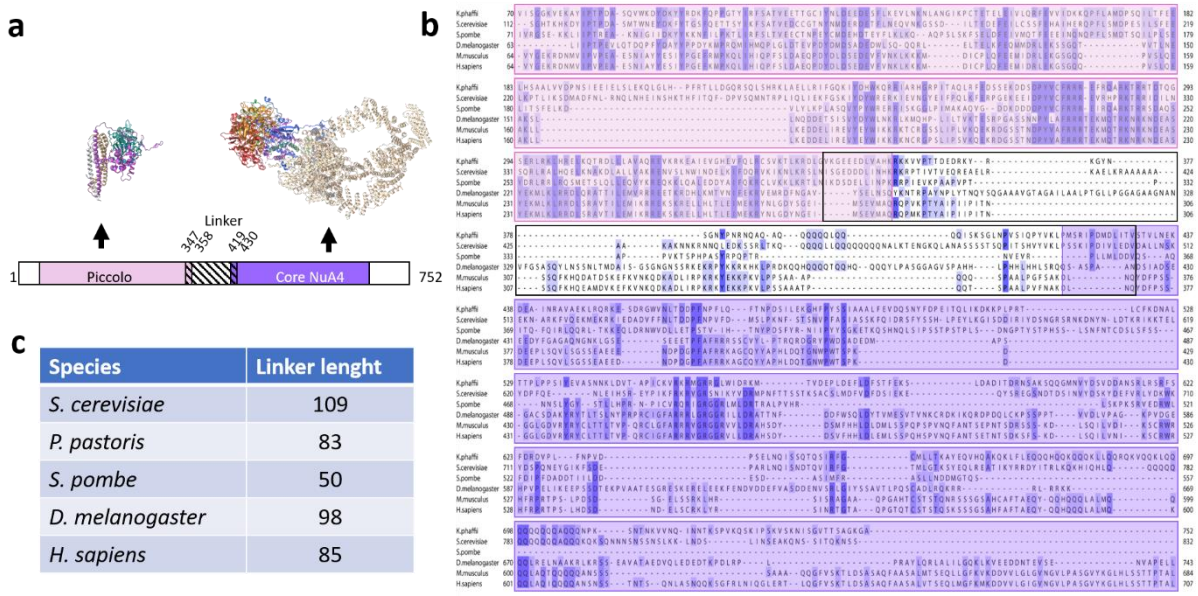

c

Species	Linker lenght
S. cerevisiae	109
P. pastoris	83
S. pombe	50
D. melanogaster	98
H. sapiens	85

Extended Data Figure 8 | domain organization and sequence alignment of the Epl1 subunit. **a**, Schematic representation of the Epl1 subunit showing in pink the N-terminal part resolved in the crystal structure of Piccolo (Xu et al., 2016a) and in violet the C-terminal part revealed in our cryo-EM map. The corresponding structures are shown and the hatched region corresponds to the unstructured linker region. Residue numbers indicate, in *P. pastoris*, the first unstructured residue in the crystal structure (347), the last residue in the crystal structure (358), the first residue in the cryo-EM map (419) and the last unstructured linker residue in the cryo-EM map (430). **b**, Multiple sequence alignment of the Epl1 subunit. **c**, table showing the Epl1 linker length in different species

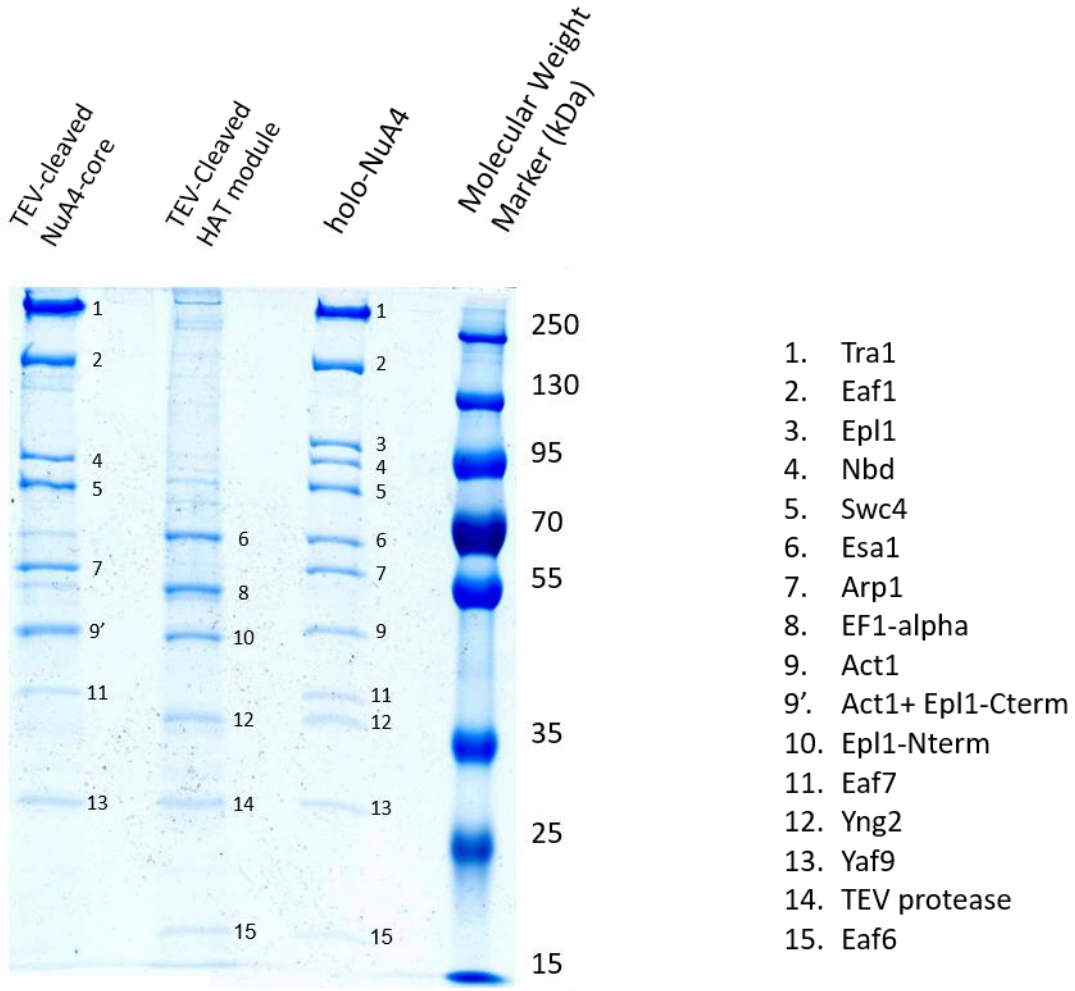

Extended Data Figure 9 | proteolytic cleavage of the Epl1 subunit to isolate the HAT module. Colloidal Coomassie blue stained SDS-PAGE analysis of a purified *P. pastoris* NuA4 complex carrying a TEV cleavage site in the linker connecting the two functional parts of Epl1. NuA4 was bound to a streptavidin column via the SBP-tag on the core Eaf1 subunit prior to addition of TEV protease. Lane 1 shows the subunits retained on the streptavidin column after TEV cleavage, Lane 2 represent the composition of the sub-complex eluted from the streptavidin column after TEV cleavage and lane 3 shows the input holo-NuA4 complex.

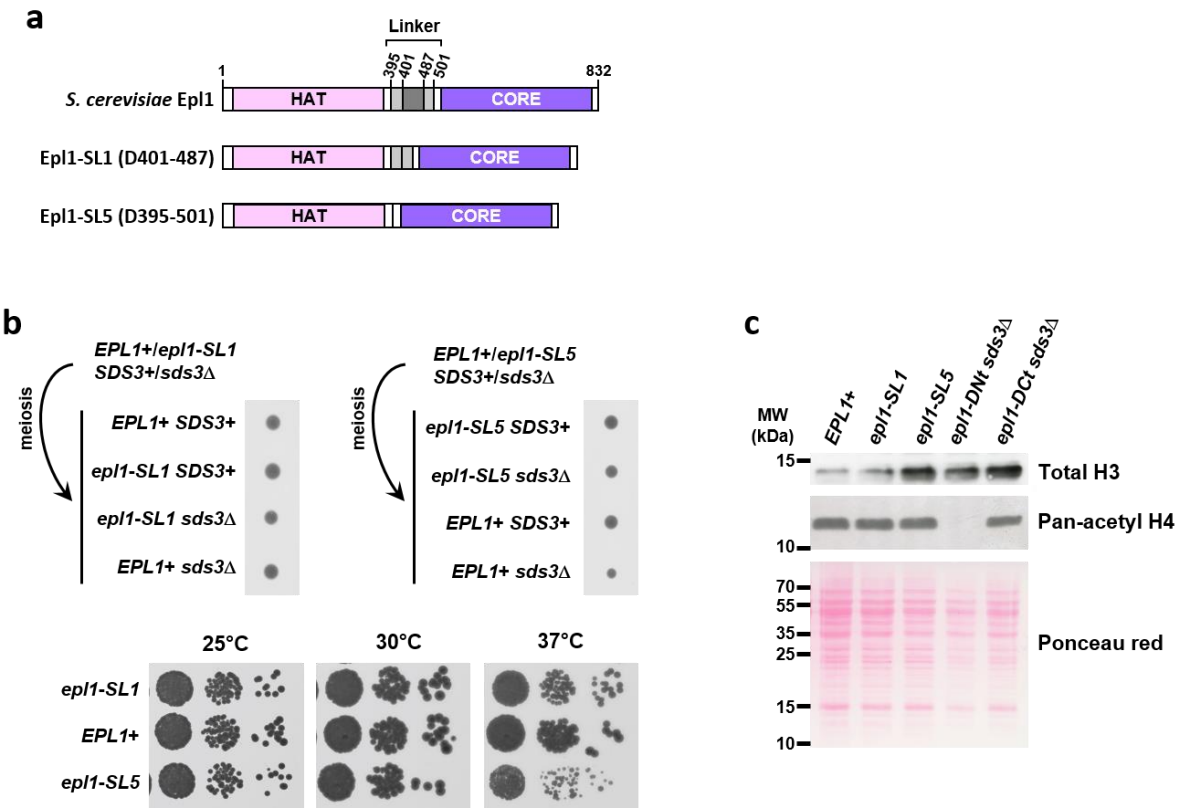

Extended Data Figure 10 | The Epl1 linker is dispensable for NuA4 activity and functions in budding yeast. a, Schematic illustration of the S. cerevisiae Epl1 linker mutants that were constructed. The *epl1-SL1* allele corresponds to a seamless deletion of residues 401-487. The *epl1-SL5* allele corresponds to a longer, seamless deletion of residues 395-501 from endogenous Epl1. **b**, *S. cerevisiae EPL1+/epl1-SL1 SDS3+/sds3*Δ and *EPL1+/epl1-SL5 SDS3+/sds3*Δ double heterozygous diploids were sporulated, dissected, and germinated to show the growth phenotype of all four possible genotypes (top panel). Single *epl1-SL1* and *epl1-SL5* mutants were isolated, along with an isogenic wild-type (WT) controls, grown to exponential phase and spotted on rich media in ten-fold serial dilutions at grown at different temperatures, as indicated (bottom panel). Data are representative of four independent experiments performed with distinct mutant clones. **c**, Acetylated histone H4 levels in exponentially growing *S. cerevisiae epl1* mutants. The control *epl1-SL1* and *epl1-SL5* single mutants were obtained from the tetrad analysis shown in C. The *epl1-DNt sds3*Δ and *epl1-CNt sds3*Δ double mutants were obtained from[32] and corresponds to a deletion of residues 1-485 and 485-833, respectively. Western blots of total protein extracts were probed with an anti-pan-acetyl-H4 antibody. An anti-H3 antibody and Ponceau red staining were used as controls for equal loading between lanes. Data are representative of two independent experiments. Source data for **c** are provided as a Source Data File.

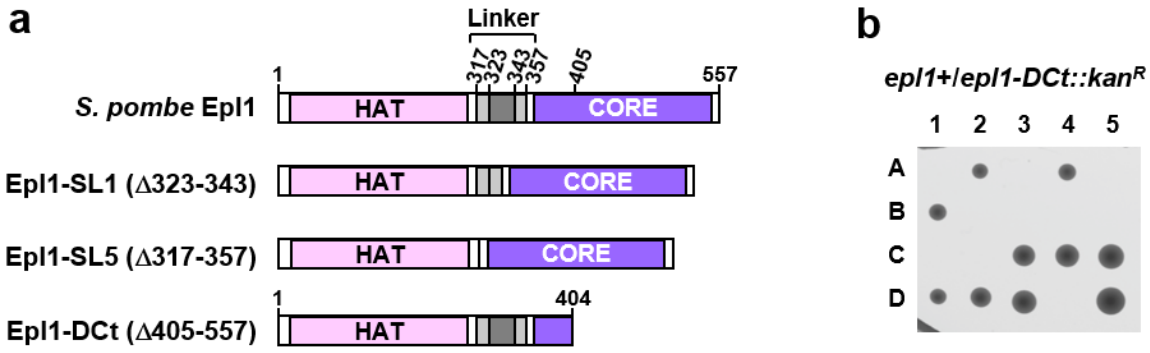

Extended Data Figure 11 | a, Illustration of *S. pombe* Epl1 mutants. The *epl1-DCt* allele has a seamless deletion from residues 405 of Epl1 until its C-terminal end (residue 557). **b**, Tetrad analysis of a heterozygous *epl1+*/*epl1-DCt* diploid strain following sporulation and germination to show 2:2 segregation of a lethal phenotype.

	NuA4-WT EMDB-15869 (overall) EMDB-15881(core)	NuA4-SL1 EMDB-15896 (overall) EMDB-15897 (core)	NuA4-SL3 PDB : 7ZVW EMDB-14989 (composite) EMDB-14980 (overall) EMDB-15066 (core) EMDB-15070 (tra1-tail) EMDB-15067 (tra1-ring)
Data collection and processing			
Magnification	105 000	81 000	81 000
Voltage (Kv)	300	300	300
Electron exposure ($e^-/Å^2$)	52.8	52.8	52.8
Defocus range (μm)	1.2-3.5	1.2-3.5	1.2-3.5
Pixel size	1.09	0.862	0.862
Symmetry imposed	C1	C1	C1
Initial particle images (no.)	350 000	1 065 689	1 250 000
Final particle images (no.)	44 000	448 963	519 840
Map resolution (Å)			
Overall	3.9	3.9	3.7
Tra1 tail			3.3
Tra1 ring			3.3
Core (Actin module, Neck, Tra1 FAT and kinase)	3.8	3.6	3.4
FSC threshold	0.143	0.143	0.143
Refinement			
Model composition			
Non-hydrogen atoms			37 825
Protein residues			4 955
Ligands			Mg : 2 ATP : 2
R.M.S. deviations			
Bond length (Å)			0.003 (0)
Bond angles (°)			0.576 (2)
Validation			
MolProbity score			1.69
Clash score			8.72
Rotamer outliers (%)			0.00
Ramachandran plot (%)			
Outliers			0
Allowed			3.43
Favored			96.57

Extended Data Table 1 | Cryo-EM data collection, refinement and validation statistics.

Strain name	Genotype	Source
DHP1475	*MATalpha, ade2-1, trp1-1, can1-100, leu2-3,112, his3-11,15, ura3, GAL, psi+*	Gift from S. Piatti
DHP1633	*MATalpha ade2-1 can1-100 his3-11,15 leu2-3,112 trp1-1 ura3-1 GAL sds3Δ::natMX EPL1-MYC13::HISMX6*	Gift from L. Pillus
DHP1634	*MATalpha ade2-1 can1-100 his3-11,15 leu2-3,112 trp1-1 ura3-1 GAL sds3Δ::natMX epl1-ΔNt-MYC13::HISMX6*	Gift from L. Pillus
DHO1635	*MATalpha ade2-1 can1-100 his3-11,15 leu2-3,112 trp1-1 ura3-1 GAL sds3Δ::natMX epl1-ΔCt-MYC13::HISMX6*	Gift from L. Pillus
DHP1655	*MATalpha ade2-1 can1-100 his3-11,15 leu2-3,112 trp1-1 ura3-1 GAL epl1-SL5-MYC13::HISMX6*	This study
DHP1661	*MATalpha ade2-1 can1-100 his3-11,15 leu2-3,112 trp1-1 ura3-1 GAL epl1-SL1-MYC13::HISMX6*	This study
DHP42	*h+N*	This study
CFP173	*h+/h- ade6-M210/ade6-M216 epl1+/epl1-ΔCt::kanMX6*	This study
DHP1236	*h+ leu1-32 ars1::pRad15-Cre-EBD-LEU2*	Derived from A9823 (R. Allshire)
CFP123	*h+ leu1-32 ars1::pRad15-Cre-EBD-LEU2 epl1-FLEx-ΔCt::natMX6*	This study
CFP129	*h+ leu1-32 ars1::pRad15-Cre-EBD-LEU2 epl1-FLEx-SL5::natMX6*	This study
CFP132	*h+ leu1-32 ars1::pRad15-Cre-EBD-LEU2 epl1-FLEx-SL1::natMX6*	This study

Extended Data Table 2 | List of yeast strains used in this study.

Strain name	Genotype	Source
DHP1475	*MATalpha, ade2-1, trp1-1, can1-100, leu2-3,112, his3-11,15, ura3, GAL, psi+*	Gift from S. Piatti
DHP1633	*MATalpha ade2-1 can1-100 his3-11,15 leu2-3,112 trp1-1 ura3-1 GAL sds3Δ::natMX EPL1-MYC13::HISMX6*	Gift from L. Pillus
DHP1634	*MATalpha ade2-1 can1-100 his3-11,15 leu2-3,112 trp1-1 ura3-1 GAL sds3Δ::natMX epl1-ΔNt-MYC13::HISMX6*	Gift from L. Pillus
DHO1635	*MATalpha ade2-1 can1-100 his3-11,15 leu2-3,112 trp1-1 ura3-1 GAL sds3Δ::natMX epl1-ΔCt-MYC13::HISMX6*	Gift from L. Pillus
DHP1655	*MATalpha ade2-1 can1-100 his3-11,15 leu2-3,112 trp1-1 ura3-1 GAL epl1-SL5-MYC13::HISMX6*	This study
DHP1661	*MATalpha ade2-1 can1-100 his3-11,15 leu2-3,112 trp1-1 ura3-1 GAL epl1-SL1-MYC13::HISMX6*	This study
DHP42	*h+N*	This study
CFP173	*h+/h- ade6-M210/ade6-M216 epl1+/epl1-ΔCt::kanMX6*	This study
DHP1236	*h+ leu1-32 ars1::pRad15-Cre-EBD-LEU2*	Derived from A9823 (R. Allshire)
CFP123	*h+ leu1-32 ars1::pRad15-Cre-EBD-LEU2 epl1-FLEx-ΔCt::natMX6*	This study
CFP129	*h+ leu1-32 ars1::pRad15-Cre-EBD-LEU2 epl1-FLEx-SL5::natMX6*	This study
CFP132	*h+ leu1-32 ars1::pRad15-Cre-EBD-LEU2 epl1-FLEx-SL1::natMX6*	This study

Extended Data Table 3 | List of oligonucleotides used for ChIP-qPCR experiments.